ABSTRACT

Title of Thesis: TEMPERATURE AND RATE DEPENDENT PARTITIONED CONSTITUTIVE RELATIONSHIPS FOR 95.5PB2SN2.5AG SOLDER ALLOY

Shirish Anurag Gupta, Master of Science, 2003

Thesis Directed By: Dr. F. Patrick McCluskey
Department of Mechanical Engineering

One of the biggest challenges for power electronic devices is to be reliable in harsh environments. The operating temperatures in typical applications can go as high as 200ºC. The die attachment material of a power electronic device is one of the weak links in the system. The eutectic Sn-Pb solder alloy, which is the most commonly used permanent interconnect in electronics packaging cannot fulfill these service requirements, hence there is a need to find suitable replacements.

Durability characterization is essential in order to accurately predict the reliability of the solder alloy chosen for the die attach material under life cycle loads. A large

number of models are available, which can be used to determine the life of die attach in small signal and power modules, however the shortfall of these models is the lack of test data for all but the most common (e.g. eutectic Sn-Pb solder) die attach materials. Hence, relevant constitutive properties must be measured, as they are essential for quantitative characterization of damage accumulated in the die attach, the knowledge of which is essential for accurate durability assessment.

The aim of this study is to determine the relevant constitutive properties for high temperature high lead 95.5Pb2Sn2.5Ag solder alloy (Indalloy 163) by implementing the direct local measurement technique. Temperature and loading rate dependent mechanical and constitutive properties of the afore mentioned solder alloy have been obtained by modeling the experimental data gathered by conducting monotonic, isothermal, constant strain rate tests at a range of temperatures and strain rates utilizing miniature single-lap shear specimens, with a partitioned form of the general constitutive equation.

TEMPERATURE AND RATE DEPENDENT PARTITIONED CONSTITUTIVE RELATIONSHIPS FOR 95.5PB2SN2.5AG SOLDER ALLOY

by

Shirish Anurag Gupta

Thesis submitted to the Faculty of the Graduate School of the
University of Maryland, College Park in partial fulfillment
of the requirements for the degree of
Master of Science
2003

Advisory Committee:

Associate Professor Patrick McCluskey
Associate Professor Bongtae Han
Associate Professor Peter Sandborn

DEDICATION

To mom and papa, for their faith in me, and for always being my number one supporters. The further I have traveled from them, the closer I feel to them. Without their support, I couldn't possibly have come this far.

ACKNOWLEDGEMENTS

Thanks are in order for a bunch of people. To the 201 community over the years, Deep, Harish, Nitin, Sumit, Vijay, Ankush, Neha, Shanon, Akanksha, and Vandana for making a lot of hard times easier by just being there. To my colleagues Karumbu, Arvind, Casey, Yunqi, Manas, Sudhir, Zeke, Christian, Luca, Will, Brian, and Witali; just working with them has been a pleasure. To Anshul, Joe, Kaushik, and Dan, for genuine support, friendship, advice, goodwill, and timely stress relief, especially Anshul, for spending endless nights working in the 'cave'…

To Dr. Kwon, for introducing me to the 'art' that is constitutive property measurement, and to Yuri, for willingly sharing her experience of testing on the Tytron. To Dr. Bongtae Han, for his guidance and understanding during the hard times. To John, Dave, and Bob at the Physics Machine Shop for their excellent workmanship and for expediting my work orders to help meet project deadlines. Thanks to Siegfried Ramminger, Siemens AG, Munich for sponsoring the die attach project, working on which has been enriching to say the least. To the faculty and staff of the department of mechanical engineering and CALCE EPSC, who help keep the program running like a well oiled machine, and to my thesis committee: Dr. Han, Dr. Sandborn, and Dr. McCluskey, for sparing their valuable time to assess my work. And most of all to my advisor, one of the nicest people I have met, for giving me enormous flexibility, humor, guidance, patience, and understanding for the past two and a half years.

TABLE OF CONTENTS

LIST OF TABLES

LIST OF FIGURES

Chapter 1. Introduction

1.1 Motivation

Electronic systems and components today are an integral part of practically every type of product, be it for an industrial, business, consumer, or military application. These electronic devices must perform the required electrical functions for which they are designed in addition to maintaining their structural integrity while being subjected to a wide range of environmental and operational loads. Common examples of loads include vibration, shock, impact, bending, radiation, moisture ingress, exposure to chemicals, and exposure to extremes of ambient and operating temperature. All electronic devices are subjected to these loads with few exceptions.

Traditionally, commercial electronic devices have been designed to operate within a small temperature range, with a maximum of 70^{o}C, or 125^{o}C for some automotive, military, and avionic applications. However, performance and reliability of power electronics systems and distributed control systems used for high temperature applications such as oil well drilling and logging, nuclear reactor monitoring, automotive engine control/monitoring, and aerospace applications, involving operating temperatures in excess of 125^{o}C (sometimes well over 200^{o}C), need to be examined. The high ambient temperatures of these applications when combined with the inherent heat generation of power electronic systems can produce a very hostile

environment for electronics, which in turn leads to significant reliability concerns, including low-cycle die attach fatigue [McCluskey et al., 1997].

Solder alloys, with high melting points are typically used in power electronic systems as a large area die attach between the silicon die and the underlying substrate. At such high operating temperatures, the common tin-lead eutectic solder cannot be used, as it would melt before fulfilling service requirements (T_m=183^{o}C). The use of high temperature solders would reduce the load on cooling systems.

Durability characterization is essential in order to accurately predict the reliability of the die attach material under life cycle loads. A large number of models are available, which can be used to determine the life of die attach in small signal and power modules, however the shortfall of these models is the lack of test data for all but the most common (e.g. eutectic Sn-Pb solder) die attach materials. To this end, relevant constitutive properties must be measured, as they are essential for quantitative characterization of damage accumulated in the die attach, the knowledge of which is needed for accurate durability assessment [Hong et al., 1995]. Solder alloys perform at relatively high homologous temperatures ($T>0.5T_m$) in typical operating conditions. Consequently, their mechanical behavior is highly nonlinear, and displays a strong dependence on loading history and environmental conditions. Hence, the behavior at different loading rates and temperatures must be analyzed. Nevertheless, there is little or no information regarding the behavior of lead-rich solders, such as 95.5Pb2Sn2.5Ag alloy. It is important to not only analyze the response of the material

to temperature but also the response to loading rate, which gives valuable information to reliability engineers in design of qualification tests. For example, temperature ramp rates of thermal cycling tests can vary from 8°C/min to 20°C/min [Jedec standard, 1989]. The temperature ramp rate can also be 50°C/min in a thermal shock test, which is used to assess the package integrity when subject to sudden temperature change [Jedec standard, 1995].

This is the first study to concentrate on the temperature and loading rate-dependent constitutive property measurements for 95.5Pb2Sn2.5Ag, a common, lead-rich, high temperature solder, used as a die attach material in power electronic systems.

1.2 Die Attach Reliability Concerns

As mentioned, one of the biggest challenges for power electronic devices is to be reliable in harsh environments. The operating temperatures in typical applications can go as high as 200ºC. Not only do these devices have to operate at harsh ambients, but also the environments are made harsher by the high power generation of devices, which can sometimes be hundreds of watts per device. This power dissipation can cause the temperature of the device to rise up rapidly when the device is switched on and drop down rapidly when the device is switched off. These rapid temperature changes upon repeated power on/off cycling can cause serious reliability concerns. Due to the rapid power and temperature cycling of the device, the die attach which connects the silicon (Si) chip to the substrate experiences high shear stresses due to

the cyclic differential expansion and contraction of the die and the substrate thereby causing damage to accumulate in the die attach.

Figures 1.1 and 1.2 below demonstrate the fundamental differences between the construction of a small signal device and a power module. The two main functions of the die attach in small signal devices are to provide mechanical support to hold the chip in place and to provide a low resistance thermal path for good heat dissipation of the device. It is important that the device provide a low impedance thermal path so that the chip temperatures are kept in range of reliable operation. In power devices, in addition to these two basic functions of the die attach there exists a third, which is to provide an electrical path to the drain on the bottom side of the device.

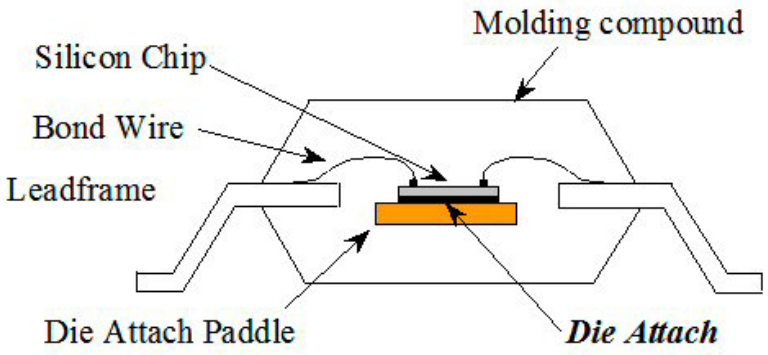

Fig. 1.1

Simple small signal device plastic package design

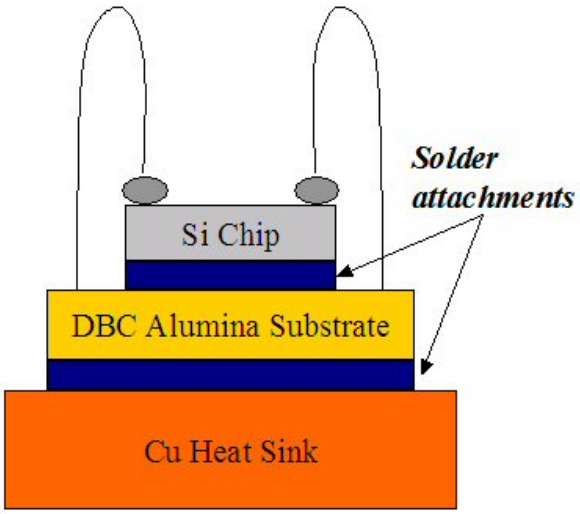

Fig. 1.2

One sided design of a power module

The ideal die attach should not only be electrically conducting, but it must also have a co-efficient of thermal expansion, which matches well with that of the die and the substrate to minimize the shear stresses it would be subject to during operation. In addition, it should be compliant enough to absorb most of the stresses instead of transferring them to the device or the substrate, which can cause additional reliability concerns such as die and substrate cracking. Some of the potential die attach materials for high temperature applications are listed in Table 1.1.

High modulus (stiff)	**Low modulus (flexible)**
Gold eutectics Silver-filled glass Silver-filled polyimides Silver-filled epoxies	Lead-tin-based solders **Lead-rich solders** Indium-based solders

Table 1.1: Die attach materials for high temperature applications.

A compliant die attach, however, is more susceptible to failure due to fatigue. The size of the die is also an important concern for reliability. Large area die attaches develop higher stresses, also making them susceptible to failure by fracture. Thus for a die size of less than 0.5cm, stiff materials like gold eutectics or silver filled glass, polyimides, or epoxies are used for better fatigue resistance. For large area die attaches in the range of $0.25cm^2$ to $6.25cm^2$, compliant attaches like lead-based or indium-based solders are used to reduce stresses in the die.

1.3 Literature Survey

Early efforts to estimate reliability of electronics systems followed a strictly statistical approach, where failure probability functions of individual components and subsystems were combined in an appropriate manner to obtain a generic model to predict the reliability of the whole system. The failure of individual components was assumed to follow the traditional *bathtub curve*. However, no understanding of the physical processes that cause these failures was included in this modeling approach. Thus this method can only be applied to specific systems, and only after relevant failure data are available. This method does not give an indication of the location or source of the failure, or its root cause.

A more fundamental approach to constitutive property characterization of permanent solder interconnections is similar to that used for traditional materials testing, viz. for structural materials such as steel and its alloys.

The traditional test methods involve the use of *bulk dog-bone* shaped cylindrical specimens, which are usually subjected only to axial displacements or loads in tension or compression. Such methods are well developed and documented in ASTM E8, E9, and E21. Various investigators have used these methods for their constitutive characterization programs [Enke et al., 1989], [Frost et al., 1988], [Jones et al., 1997], because of their relative ease of adaptability. Methods involving the use of such bulk specimens neglects some fundamental aspects of application of these materials as interconnects in electronics packaging. The dominant mode of deformation in solder die attachments is shear due to differential thermal expansion of the die and the substrate. Additionally, the volume of metal used in permanent interconnects are small. Thus material response to load may be different for miniature interconnects as compared to bulk specimens. Some researchers have performed tests to exclusively compare the response of bulk specimens and miniature specimens. Raeder et al. [1994] showed that single-lap shear joints of eutectic Sn-Ag solder are significantly stronger than bulk specimens of the same material. Joint strengthening due to dispersion of intermetallic layers in bulk solder, differences in grain size and resultant creep deformation mechanisms, and geometry constraints in small joints or those with high aspect ratios may also cause discrepancies in bulk solder and miniature specimen behavior [Yang et al., 1996]. Thus it may be more appropriate to test solder specimens that have length scales that are close to those of actual large area die attaches. This has inspired investigators to use miniature specimens in their experimental programs.

Other investigators have taken alternative approaches to constitutive property measurement of solder alloys. A large number of programs utilize actual package architectures [Darveaux, 1992], [Solomon, 1990], [Grivas et al., 1979], [Kashyap et al., 1981], [Lam et al., 1979]. One approach uses ball indentation techniques to measure constitutive properties such as hardness [Giannakopoulos et al., 1999; Mahidhara et al., 1996].

In any successful approach, documentation of specimen preparation is critical. Microstructure of as-cast and aged specimens can differ significantly thus altering its mechanical response to loading, leading to variation in test data. As a result, the specimen preparation procedure including the reflow profile and subsequent processing steps must be kept standardized as far as possible throughout the course of the testing program.

1.4 High Temperature Pb-based Solders

Before a solder alloy is chosen for service, it must satisfy a range of qualifications. In addition to being cheap, it should be easily available and easily adaptable to existing manufacturing processes. The solder should be compatible with other materials used in the assembly. And finally, and most importantly, the solder fatigue properties must be sufficient to satisfy the design requirements of the assembly. The choice of solder alloy thus becomes an increasingly important issue, as it will depend on the service

requirement it is meant to fulfill. For example, 63Sn37Pb cannot fulfill service requirements of 200^{o}C operating temperature, since it has a melting point of 183^{o}C. Rather, materials with a melting point well above 200^{o}C, such as lead-based, lead-rich solders would be more suitable.

Phase transition temperatures of a few lead-based high temperature solders are included in Table 1.2 [Hwang, 1996]. For practical applications three distinct temperatures are used. *Liquidus* temperature is defined as the temperature, above which the solder alloy is in stable liquid phase. *Solidus* temperature is defined as the temperature, below which the solder alloy is in stable solid phase. *Plastic Range* is defined as the temperature range between the solidus and liquidus temperatures of the given composition, for which both the solid and liquid states co-exist in equilibrium in the solder alloy. *Eutectic* temperature is defined as the temperature, at which a single liquid phase is transformed into two solid phases.

Alloy Composition	**Solidus (^{o}C)**	**Liquidus (^{o}C)**	**Plastic Range (^{o}C)**
37Pb/63Sn (E*)	183	183	0
90Pb/10Sn	268	302	34
95Pb/5Sn	308	312	4
70Pb/30In	240	253	13
88.9Pb/11.1Sb (E)	252	252	0
97.5Pb/2.5Ag (E)	303	303	0
43Pb/43Sn/14Bi	144	163	19
20Pb/34Sn/46Bi (E)	100	100	0
92Pb/5Sn/3Sb	239	285	46

Alloy Composition	Solidus (^oC)	Liquidus (^oC)	Plastic Range (^oC)
18Pb/70Sn/12In (E)	162	162	0
92.5Pb/5In/2.5Ag (E)	300	300	0
36Pb/62Sn/2Ag (E)	179	179	0
92.5Pb/5Sn/2.5Ag	287	296	9
93.5Pb/5Sn/1.5Ag	296	301	5
95.5Pb/2Sn/2.5Ag	***299***	***304***	***5***
97.5Pb/1Sn/1.5Ag	309	309	0

Table 1.2: Phase transition temperatures of a few Pb-based solder alloys [*Note: (E) – eutectic alloy]

1.5 Organization of Thesis

Chapter 2 explains the Direct Local Measurement Technique (DLMT) developed by Kwon et al. [2003] for the constitutive property measurements of lead-free solder alloys used as permanent interconnections in Surface Mount Technology (SMT).

Chapter 3 describes the implementation of the DLMT for constitutive property measurements of lead-rich 95.5Pb2Sn2.5Ag solder alloy used as a large area die attach in power packaging.

Chapter 4 shows the experimental results of monotonic, isothermal, constant strain rate testing of 95.5Pb2Sn2.5Ag solder. Temperature and loading rate-dependent mechanical properties such as Yield stress and Ultimate tensile strength are obtained, in addition to the temperature and loading rate-dependent elastic, plastic, and creep properties. Creep model predictions are compared with experimental results.

Diffusion mechanisms for creep deformation are discussed and the diffusion mechanism(s) responsible for creep deformation in 95.5Pb2Sn2.5Ag solder, for the given test conditions, is identified.

Conclusions provide a summary of the thesis and the contributions. A list of relevant books and articles is also provided for reference.

Appendix A contains detailed procedures for safe operation of the MTS Tytron^{TM} 250, in addition to relevant tuning and testing procedures.

Chapter 2. Test Methodology: Direct Local Measurement Technique for Constant Strain Rate Testing

Solder alloys perform at relatively high homologous temperatures in typical operating conditions. Consequently, their mechanical behavior is highly nonlinear, and displays strong dependence on a loading history and environmental conditions. Thus, temperature and loading rate-dependent constitutive properties of solder alloys are important for accurate stress analysis, which are subsequently used to assess damage accumulation due to life-cycle stresses.

The following sections of this chapter describe the Direct Local Measurement Technique (DLMT) developed for constitutive property measurements of lead-free solder alloys used as permanent interconnects in surface mount technologies [Lee et al., Mar 2002; Lee et al., Oct 2002; Kwon et al., 2002; Kwon et al., 2003].

2.1 Specimen Configuration

As explained in Section 1.4, traditional testing methods involving the use of bulk specimens neglect some fundamental aspects of material behavior when using solder alloys as permanent interconnects in electronics packaging. The dominant mode of failure in the actual permanent solder interconnect is shear, due to thermal expansion mismatch between the die and the substrate. Also, the volume of the solder alloy in these electronic assemblies can be extremely small. The properties of solder

interconnects are strongly dependent upon grain structure, which is governed by the fabrication temperature and the joint size. It is desirable that the specimen be fabricated under conditions as similar to the assembly reflow process as possible and that its size is on the same order of the actual solder joints. For this reason, a conventional simple tension test is not suitable for measuring the constitutive properties of solder alloys. Miniature lap shear specimens better simulate the geometrical and loading constraints of the permanent solder interconnects in actual applications. Miniature specimens can have a single joint (single-lap shear), or two joints (double-lap shear), or have multiple joints (arrayed-lap shear; flip-chip array). Iosipescu [1967] has designed a specimen for single in-plane shear of metals or composites utilizing a notched beam type sample, which is loaded so as to produce a zero bending moment across the notch or test section. A typical Iosipescu specimen is shown in Figure 2.1.

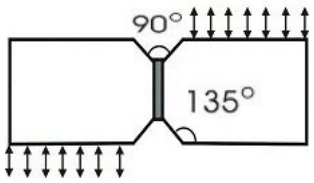

Fig. 2.1
Iosipescu Uniform Shear Specimen Configuration

Kwon et al. [2003] have improvised the modified Iosipescu micro-shear lap specimen [Reinikainen et al., 2001] for uniaxial testing purposes. This specimen configuration is shown in Figure 2.2; it retains the characteristic Iosipescu V-notch, which helps minimize stress concentration at the edges and helps maintain a uniform shear stress

within the solder, while at the same time permits it to be mounted on a uniaxial test frame. Kwon et al. [2003] have used a nominal joint height of 300μm to simulate the geometric and loading constraints present in a solder bump. Nominal solder joint dimensions are: 2.0mm x 1.5mm x 0.3mm.

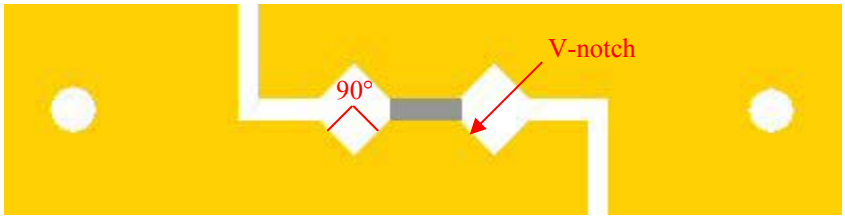

Fig.2.2
Specimen Configuration

2.2 Specimen Preparation

Good wetting of the solder to the copper requires the active surfaces be thoroughly cleaned. Use of well-aligned and symmetric specimens with good axial linearity and surface planarity reduces the stress developed simply through installing the specimen into the test fixture on the machine. This simplifies the stress fields throughout the solder thereby producing more uniform test data [Haswell, 2001]. Specimens are only produced one at a time. Thus, it is imperative that the procedure be quick, repeatable, and consistent. To this end, specimens are thoroughly cleaned with isopropyl alcohol (IPA) and a special-purpose soldering fixture is designed for reflowing the solder joint. Steel shims are wedged between the platens to maintain a joint height of 300μm. The key-shaped platens are made of cold-rolled copper and are obtained via wire cutting (EDM).

Cleaning

The active surface of the platen (surface eventually in contact with the solder joint) is made smooth using medium grade sandpaper. The platens are then dipped into flux, and heated to activate the flux. The copper platen is brushed clean with IPA to remove all debris on the surface. This step may be repeated as required.

Sealing

Silicone rubber is applied to the V-notch to prevent the flowing of solder down the slope of the V-notch during reflow. The silicone rubber is left to cure for 12 hours.

Reflow Soldering

The platens are then located on the soldering fixture. The active surfaces are again dipped in flux, which is activated as before. The fixture with the two key-shaped platens is then placed on a hotplate, at 250°C, well above the melting point of the alloy. The solder wire is brought in contact with the active surface, which is at a temperature sufficient to melt the solder on contact and the solder fills the gap by capillary action, creating the joint. The specimen is then gradually brought down to room temperature using a thick aluminum cold plate as a heat sink. Specimens are visually inspected for alignment and solder volume.

Polishing

Specimens are then polished mainly for two reasons: first, to reduce the specimen to the desired thickness, and second, for axial linearity and surface planarity. Two specimens are simultaneously mounted on a special-purpose polishing fixture to increase planarity by increasing the bearing surface, and making it easier to maintain orthogonality of the specimen during polishing. The specimen is polished on both

sides using multiple grades of waterproof metallurgical sandpaper (600, 800, and 1200 grit) from coarse grade to remove excess solder to fine grade for a highly polished surface.

Inspection and Measurement of Joint dimensions

The specimen is inspected under an optical microscope for defects such as cracks or surface voids and photographed for documentation purposes. Actual joint dimensions are measured using digital micrometers and an optical microscope.

Pin press-fitting

If the specimen passes the visual inspection, holes in the copper platens are press fitted with pins, which are used for mounting *extensions* (Please refer to section 2.4 for details).

Inspection

The specimen is again viewed under the microscope for any evidence of stress-related damage to the joint due to press fitting.

Attaching extensions

The extensions are mounted using room temperature curing high temperature epoxy, after which the epoxy is left to cure for 24 hours. The specimen is now ready for testing.

2.3 Test Equipment – MTS Tytron^{TM} 250 MicroForce Testing System

Since typical solder interconnects in modern electronics are small, measuring the mechanical behavior is a significant engineering challenge. The solder joint height is

very small (usually less than 500μm), and shear deformation is dominant. Most specimens therefore require a very small gauge length. Displacement sensors or gauges, which are easy to use with bulk specimens are often too cumbersome to be used with these miniature specimens. Due to the small axial displacements recorded in miniature specimens, the large gauge length and poor resolution of typical displacement sensors induce errors in capturing meaningful test data. Such factors contribute towards the choice of testing equipment to be selected for use. A micro-mechanical tester is employed to document the solder deformations.

The MTS Tytron^{TM} is a uniaxial micro-tester for miniature specimens. It has a load capacity of 250N and a load resolution of 0.001N. The system consists of the Tytron 250 load unit, the power amplifier, the Teststar IIs digital software, and the Teststar system software. Figure 2.3 shows the system components.

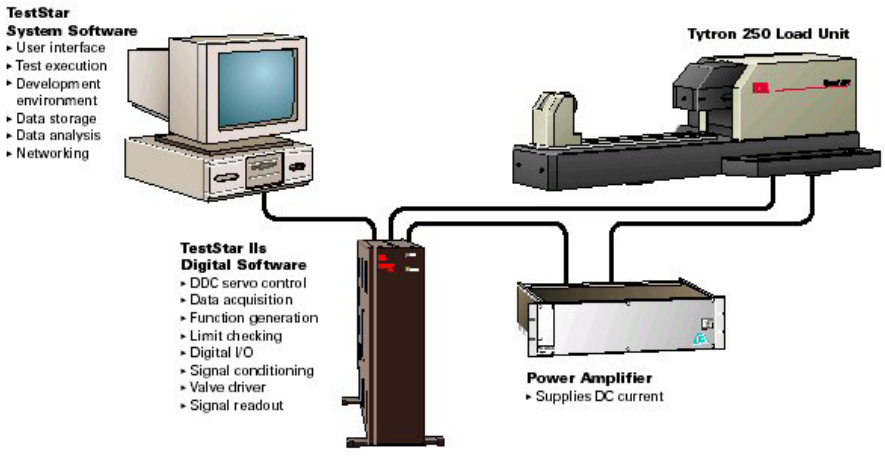

Fig. 2.3
The MTS Tytron^{TM} System

The main hardware components of the load unit are the actuator, the reaction fixture, the force transducer, and the measurement devices. A directly coupled linear DC Servomotor drives the actuator, which is capable of speeds ranging from 1μm/hr to 0.5m/sec. It has a stroke of 100mm and is capable of frequencies of upto 50Hz. The force transducer is mounted on the reaction fixture and is stationary. There are two force transducers, with load capacities of ±10N (resolution: 0.0003N) and ±250N (resolution: 0.0076N). There are three measurement devices besides the force transducers, namely the linear variable differential transformer (LVDT), the displacement gauge, and the miniature axial extensometer. The various components of the load unit are depicted in Figure 2.4.

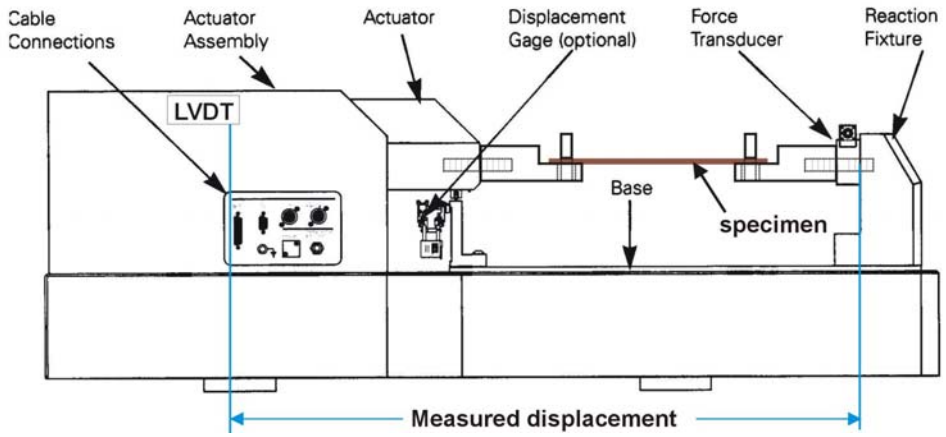

Fig.2.4

MTS Tytron™ Testing System Test Configuration

The LVDT is mounted on the actuator and measures displacement between the actuator and the reaction fixture. It has a resolution of 1.83μm for the ±60mm displacement range, and a resolution of 0.153μm for the ±5mm displacement range. It must be kept in mind that when using the LVDT for measurement, the effect of the

compliance of the entire load train must be accounted for and subtracted from the measured displacement. The displacement gauge has a much higher resolution of 0.061μm for a ±2mm displacement range. The third device is the miniature extensometer, which is by far the most accurate and useful since it makes direct strain measurements possible, thus eliminating the compliance effects of the load train. The extensometer (632.29F-20) has a 3mm gauge length and a resolution of 2.44με (0.0732μm) for the ±8% strain range and a resolution of 0.244με (0.00732μm) for the ±0.8% strain range. In addition to these components, the Tytron™ also has a temperature controller and a temperature chamber. The temperature controller can provide a temperature range of –75°C to 200°C and can control the temperature to within ±1°C.

Detailed procedures for the safe operation of the MTS Tytron™ 250 Tester are explained in Appendix A, along with the relevant testing procedures used for experimentation in this study.

Due to their small size, the axial stiffness, or compliance, of miniature specimens can be very high compared to bulk specimens, thereby increasing the effect of the compliance of the machine frame and load train on the experimental data. This necessitates local measurement of solder deformation.

2.4 Direct Local Measurement of Strain Using Axial Extensometer

Conventionally, a shear lap test is performed using a uniaxial testing machine and the measured uniaxial displacements are converted to shear displacements. The total displacement captured by the displacement gage includes displacements of other deformable bodies in the system and they must be compensated to obtain the true deformation of solder. The compensation should include machine compliance, grip compliance and copper compliance.

The strain gauge or extensometer is used to measure a displacement over a small gage length in the uniaxial tension test. For a shear lap test, however, they cannot be applied directly on the specimen since a relative displacement between the top and bottom of the test coupon is to be measured. An auxiliary device has been developed to cope with the problem. The device (referred to as *extension unit*) is attached directly to the specimen. An extensometer is mounted on the extension unit and it permits the shear displacement of the solder to be measured as an equivalent axial displacement by the extensometer.

The experimental setup with extensions and an extensometer is shown in Figure 2.5. A high-resolution miniature extensometer (MTS 632.29F-20) is attached to the units by two rubber bands.

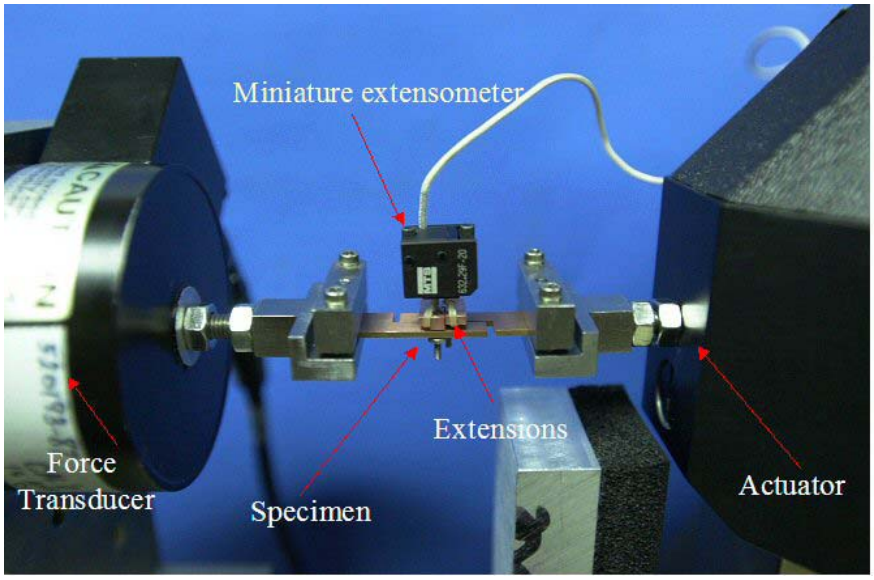

Fig. 2.5

Extensions attached to specimen: Set-up

Figure 2.6 illustrates how the unit is attached to the shear specimen. A pair of dowel pins is inserted in the specimen by press fitting and the units are attached to the other end of the pins using a room temperature curing high temperature epoxy adhesive. With this configuration, the right-hand side unit has a relative horizontal motion with respect to the left-hand side unit. When an extensometer is mounted in such a way that each knife-edge is on each unit, the extensometer effectively measures the relative displacement between the units, which can be related to the shear displacement of the solder joint.

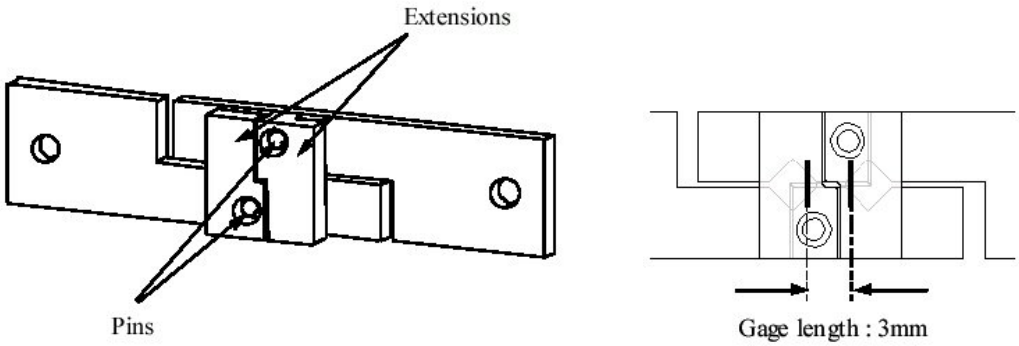

a) b)

Fig. 2.6

Extensions attached to specimen: Schematic

The extensions are designed in such a way that the knife-edges of the extensometer are exactly aligned with the pinholes of the extensions. The reason for this is simple; the two extensions fixed atop the specimen do not come in contact with each other and are free to translate along with the copper platen they are fixed to. In this way, the extensometer is able to measure the deformation between the two pinholes on either platen of the specimen, shown by points B and B' in Figure 2.7.

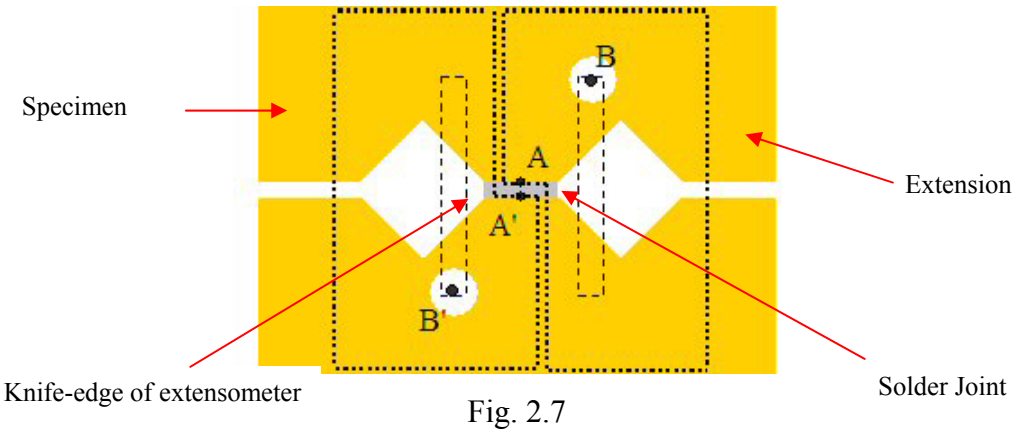

Fig. 2.7

Extensions superimposed on specimen

B & B' – at location of pins

A & A' – at Cu/solder interface

The extensometer measures the deformation between B and B'. But what is actually required is the deformation between A and A', i.e. the actual deformation of the solder joint. To put it simply, we need to find out the deformation between points A and B, i.e. the deformation of the copper, and for that matter between A' and B' (same), and subtract this apparent deformation from the measured deformation to obtain the actual solder deformation.

2.5 Subtraction of Compliance Effects of Copper

This section explains the methodology proposed by Kwon et al. [2003] for subtracting the effects of copper compliance on the deformation measurements made using the extensometer to obtain actual solder deformation. Finite element analysis is used to subtract the compliance effects of copper from the measured deformation. For

sake of convenience, the various terms used in this section are given the following notations:

- Actual deformation of copper: δ_{AB}
- Shear deformation of solder: $\delta_{AA'}$
- Corrected deformation measured by extensions: $\delta_{BB'}$
- Applied Force: F_{app}
- Compensation Rate: $CR(Cu)$
- Deformation measured by extensions: $\delta_{\exp}$
- Rotational correction factor applied to deformation measured by extensions: δ_{θ}
- Apparent deformation of copper: δ_{app}
- Rotational correction factor applied to apparent deformation of copper: δ_{rot}

The shear deformation of solder can be obtained by subtracting the compliance effects of copper from the measured deformation,

$$\delta_{AA'} = \delta_{BB'} - 2\delta_{AB} \tag{2.1}$$

Let us define a point C on the periphery of the specimen and let us name the center point of the solder joint to be S as shown in Figure 2.8. Rotational effects become

more and more pronounced as one moves from the point S towards the point B. Therefore, the extensometer overestimates the deformation between points B and B'.

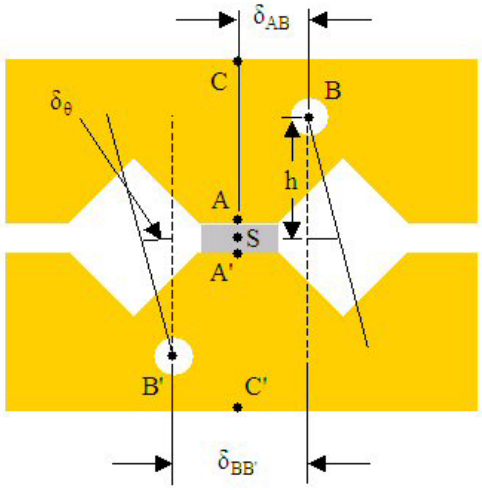

Fig. 2.8

Subtracting the effects of copper compliance on measurement of solder deformation

A rotational correction factor is applied to the measured deformation to obtain the true measured deformation.

$$\delta_{BB'} = \delta_{\exp} - 2\delta_{\theta} \tag{2.2}$$

Similarly, in an effort to estimate the actual deformation of copper, one must subtract the rotational effects from the apparent deformation of copper. Therefore,

$$\delta_{AB} = \delta_{app} - \delta_{rot} \tag{2.3}$$

θ_A, θ_B, θ_C, and θ_S are the rotational angles of points A, B, C, and S, which are used for calculation of the above rotational correction factors. Finite element analysis (FEA) using the tool ANSYS® is employed to simulate the deformation of the specimen under the application of an arbitrary force. Once all these above factors have been calculated for a particular specimen thickness, the compensation rate can be calculated by the formula:

$$CR(Cu) = \frac{2\delta_{AB}}{F_{app}} \tag{2.4}$$

The finite element model may be solved for different values of thickness, and a plot of compensation rate, defined as the compensation displacement per unit load, as a function of the specimen thickness may be obtained.

This plot serves as a quick calculator of the compliance effects of the copper on the deformation of the solder joint, for any specimen thickness, and can be immediately subtracted to obtain shear deformation of solder. This is demonstrated by equations (2.5) and (2.6).

$$\delta_{AA'} = \delta_{\exp} - 2\delta_{AB} \tag{2.5}$$

where

$$\delta_{AB} = F_{app} \times CR(Cu) \tag{2.6}$$

It is important to note that the displacement to be compensated is only a function of applied load and axial stiffness of the copper. The modulus of copper is obtained experimentally using a copper strip specimen with a strain gage. The stress and strain values are determined from the applied force and solder displacement respectively.

2.6 Constitutive Modeling

The stress-strain behavior for engineering materials is fairly complicated, and depends on several factors, with temperature, strain (deformation) rate, and strain history being the most important. An early concept in developing constitutive equations was the idea that the flow stress was dependent only on the instantaneous values of strain, strain rate, and temperature [Dieter, 1986].

$$f(\sigma, \dot{\varepsilon}, \varepsilon, T) = 0 \tag{2.7}$$

However it was soon realized that plastic deformation is an irreversible process. The flow stress depends fundamentally on the dislocation structure, which depends on the *metallurgical history* of strain, strain rate, and temperature. The general form of a constitutive equation is given by,

$$d\sigma = \left\{\frac{\partial \sigma}{\partial \varepsilon}\right\}_{\dot{\varepsilon}T} d\varepsilon + \left\{\frac{\partial \sigma}{\partial \dot{\varepsilon}}\right\}_{\varepsilon T} d\dot{\varepsilon} + \left\{\frac{\partial \sigma}{\partial T}\right\}_{\varepsilon\dot{\varepsilon}} dT \tag{2.8}$$

where ε is the uniaxial or equivalent strain, σ is the equivalent stress, T is temperature, and $\dot{\varepsilon}$ is the strain rate.

From a very basic perspective, deformation can be classified into two types, namely recoverable elastic deformations and non-recoverable inelastic deformations. Recoverable, in this case, means complete and instantaneous time-independent elastic recovery although certain amount of anelastic i.e. time-dependent elastic recovery does take place as well [Arrowood et al., 1991]. However, for all practical purposes elasticity is described by a simple linear relationship between the applied stress and measurable deformation, which is known as Hooke's law:

$$\varepsilon_{el} = \frac{\sigma}{E(T)} \tag{2.9}$$

where E is the temperature dependent Young's modulus of elasticity, σ is the equivalent stress, and ε is the uniaxial or equivalent strain.

$$E(T) = E_0 - E_T(T) \tag{2.10}$$

where T is the temperature. For most engineering materials and all solders, the elastic modulus is temperature and strain rate dependent [Lau & Rice, 1992].

Modeling the inelastic behavior is far more complex, since it involves plastic and creep deformation interactions. For the sake of convenience, plasticity is modeled as a pseudo-instantaneous phenomenon, i.e. it is assumed to be time-independent, whereas creep is time-dependent. Time-independent plasticity is typically modeled using a power-law expression, commonly known as the Exponential Hardening model:

$$\sigma = K(\varepsilon_{pl})^{n_p} \tag{2.11}$$

where $\sigma > \sigma_y$ and σ_y is the yield stress, K is the pre-exponential strength (hardening) coefficient, and n_p is the plastic strain hardening exponent, which are modeled as temperature dependent constants. Plastic deformations take place in conditions wherein there is insufficient time for time-dependent deformation to occur, i.e. at relatively higher strain rates. Since creep is a thermally activated process, plastic deformation is prominent at low temperatures. Plastic behavior has a strong dependence on temperature and strain rate.

However, since solders alloys are used at high *homologous* (T/T_m) temperatures, even at room temperature, i.e. $T>0.5T_m$ (T_m – melting point), more emphasis is placed on creep deformation. A generalized scheme for modeling creep deformation is shown in Figure 2.9. Accumulation of creep deformation can be divided into three steps. The strain rate starts high (primary creep), but decelerates into a lower, steady state value. This is the region where the creep strain rate is saturated and is known as steady state creep strain rate (secondary creep). Eventually, the strain rate begins to increase

rapidly eventually leading to failure by creep rupture (tertiary creep). The secondary creep strain region is the one that is most often modeled, and chosen to represent the entire creep process; the reason being that modeling steady state creep eliminates the need for inclusion of strain history.

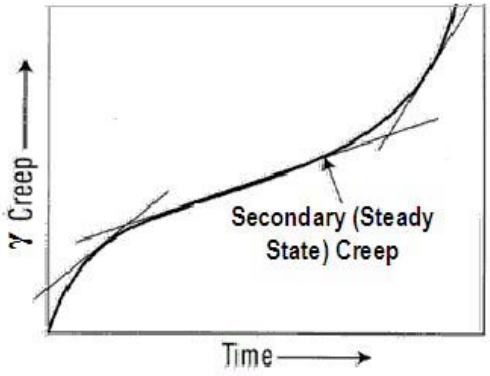

Fig.2.9
Typical constant load creep test

Weertman's steady state power law is used for modeling the steady state, secondary creep strain rate [Tribula & Morris, 1990; Pao et al., 1993]:

$$\dot{\varepsilon}_{cr} = A\sigma_v^{\frac{1}{n_c}} e^{\frac{-Q}{RT}} \qquad (2.12)$$

where A is the stress co-efficient, $1/n_c$ is the creep strain hardening exponent, Q is the thermal activation energy of creep, R is the Bolztmann constant, T is the absolute temperature, $\dot{\varepsilon}_{cr}$ is the equivalent creep strain rate, and σ_v is the equivalent saturation creep stress.

Various other steady-state creep models employed in the literature include the hyperbolic sine [Wang et al., 1998; Darveaux et al., 1993; Frear et al., 1996], the Norton model [Mukai et al., 1998; Hall, 1987], variations of the partitioned creep model [Wong et al., 1988; Shine et al., 1988], variations of the Sherby-Dorn model [Kashyap et al., 1981; Langdon et al., 1977]. Other investigators chose to model the primary creep behavior [Darveaux et al., 1997], which can be significant in certain conditions. In some cases, plasticity can be represented in a unified manner, using a single expression to represent both the time-independent and the time-dependent deformation. Examples of this type of modeling scheme are the Bodner-Partom unified creep-plasticity model [Skipor et al., 1996], and the Anand model [Anand, 1982; Wilde et al., 2000].

Thus, by adding the separately calculated elastic, plastic, and creep deformation, the partitioned constitutive relationship gives us the total strain and is given by,

$$\varepsilon_{tot}(t) = \varepsilon_{el} + \varepsilon_{pl} + \varepsilon_{cr}(t) \tag{2.13}$$

where ε_{tot} is the total deformation of the solder joint, ε_{el} is the time-independent elastic deformation, ε_{pl} is the time-independent plastic deformation, and ε_{cr} is the time-dependent creep deformation, which can also be expressed as,

$$\varepsilon_{tot}(t) = \frac{\sigma}{E(T)} + \left(\frac{\sigma}{K(T)}\right)^{\frac{1}{n_p(T)}} + tA(\sigma)^{\frac{1}{n_c}} e^{-\frac{Q}{RT}} \qquad (2.14)$$

where is ε the equivalent strain and σ is the equivalent stress.

2.7 Experimental Procedures – Determination of Constants

The values of the material constants in the constitutive model developed above are obtained experimentally. A test matrix is developed to determine the time independent behavior (elastic and plastic) and time dependent creep behavior. The tests are conducted for a range of constant strain-rates and temperatures. The procedure for determining the elastic, plastic and creep properties is explained below.

2.7.1 Time-independent Elasticity - Modulus Test

Isothermal monotonic tests are conducted in strain control mode to obtain the linear load-displacement curve. After the first measurement, the specimen is flipped and measured again. The two values are averaged to negate the effect of misalignment. The elastic modulus of solder alloys is a function of strain rate as well as temperature [Shi et al., 1999]. However, the strain rate effect on modulus is not investigated here. A shear strain rate ($\dot{\gamma} = 1 \times 10^{-3} s^{-1}$) is used for modulus tests because it is reasonably close to the actual strain rate of solder in microelectronic packages under normal operating conditions. Modulus tests are performed for a temperature range designed to simulate field-loading conditions. For the tests at the elevated temperatures, an

environmental chamber is placed at the test section to maintain the test temperature, and the grips with longer rods are installed to connect the specimen to the testing machine. The long arm makes an initial alignment more difficult. A copper strip with strain gages on both sides is used to help the initial alignment. Due to the extremely small strain to be measured for the modulus test, specimen-to-specimen variations are often observed. Tests are conducted on several specimens to check for consistency of data. The raw data is averaged to minimize possible random errors.

After subtracting the compensation displacement, the true load-displacement curve is obtained. It is then converted to the shear stress-shear strain curve using the geometrical parameters of the solder joint, from which the shear modulus can be determined. Subsequently Young's modulus can be calculated by using the relationship of the elastic constants, assuming a suitable value for the Poisson ratio, ν, using engineering judgment.

2.7.2 Time-independent Plasticity - Constant strain rate test

Implementing the constant strain rate test has advantages over the creep (constant load) test. With the constant strain rate test, rate-dependent properties as well rate-independent properties can be determined, which can reduce the total number of tests significantly. Another practical advantage is that undesired data can be screened out at the early stage of the tests. If the specimen has defects and thus a crack grows during the test, a significant load drop is visible in the load-displacement curve. Also,

since a low strain rate test usually runs for 40~60 hours, it is extremely time-effective if the specimen with defects is detected at the early stage of test.

The tests are conducted for a range of constant strain rates at the pre-determined temperatures. For the constant strain rate tests, the bending effect associated with misalignment of the specimen is not significant because sufficient plastic flow occurs during the test to eliminate the effect [ASTM Std E1012-99].

Separating the plastic flow into an effectively strain rate-independent stress-strain curve and strain rate-dependent plastic flow processes is difficult. One way to get an approximately strain rate-independent curve is to extrapolate the flow stresses vs. strain rate curve at each value of strain to very high strain rates where the increase in the flow stress is minimal for the corresponding strain rate. Defining the extrapolated value of flow stress at a very high strain rate to be the true unrelaxed stress for a given value of strain, and finding such a value for different values of strain allows one to obtain a stress-strain curve that is approximately *strain-rate independent* [Mavoori et al., 1997].

Shear stress can then be converted into an equivalent tensile stress and shear strain to an equivalent tensile strain by applying the Von Mises yield criterion to obtain the relationships [Meyers et al., 1984],

$$\sigma = \tau\sqrt{3}, \varepsilon = \frac{1}{\sqrt{3}}\gamma \tag{2.15}$$

From the data obtained through the above method, the time-independent exponential hardening constant and the pre-exponential co-efficient can be calculated by curve fitting.

2.7.3 Time-dependent Creep – Constant Strain Rate Test

In general, time-dependent creep behavior can be characterized by a data set consisting of a steady-state strain rate and a saturation stress. The data are usually obtained from creep (constant load) tests. In creep tests, the strain rate is constant in the secondary (steady-state) creep regime, at a constant applied load. In this research, however, constant strain rate tests were conducted to obtain the data set. In a constant strain rate test, the load increases at a constant strain rate, and eventually the flow stress reaches its steady state saturated value, and is constant.

The tests are conducted at a range of temperatures and strain rates. After converting the shear components into the equivalent tensile components, saturation stress and strain rate pairs obtained from the constant strain rate tests at different temperatures were plotted on a log-log scale. The creep exponent, the stress co-efficient, and the thermal activation energy for creep can be calculated as follows,

$$\ln \dot{\varepsilon}_{cr} = \ln A - \frac{Q}{RT} + \frac{1}{n_c} \ln \sigma_v \qquad (2.16)$$

The constant term, $\ln A - \frac{Q}{RT}$, can be decomposed into the co-efficient and the activation energy by plotting vs. the inverse of temperature. The y-intercept gives the co-efficient and the slope gives the activation energy.

This methodology has been implemented successfully for constitutive property measurement of lead free solder alloys used as permanent interconnects in surface mount technologies. However, modifications are required before this methodology can be adapted for the determination of the constitutive properties of high temperature, high lead solder die attaches such as the 95.5Pb2Sn2.5Ag alloy. These issues are addressed in Chapter 3.

Chapter 3. Implementation of Direct Local Measurement Technique for Constitutive Property Measurements of 95.5Pb2Sn2.5Ag Solder Alloy

The following sections of this chapter describe the implementation of the Direct Local Measurement Technique for constitutive property measurement of 95.5Pb2Sn2.5Ag solder alloy, used as a large area die attach in power packaging.

3.1 Modification of Specimen Geometry

In this study, a nominal joint height of 100μm was used to simulate the geometric and loading constraints present in a large area die attach. Nominal test specimen solder joint dimensions were: 2.0mm x 1.5mm x 0.1mm. Figure 3.1 shows the specimen configuration used.

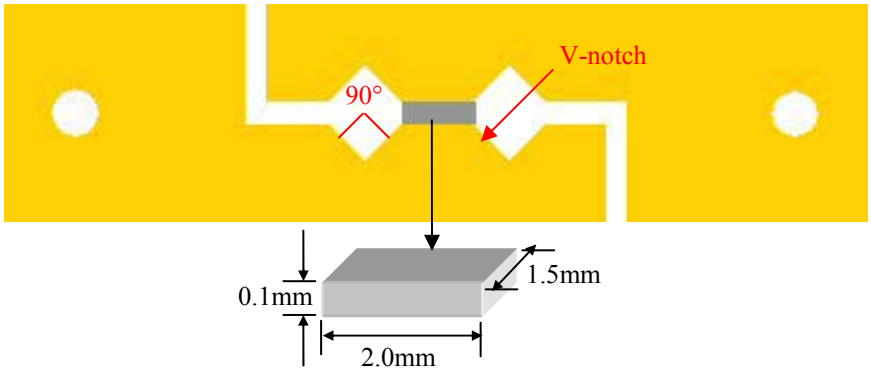

Fig. 3.1
Specimen Configuration with Modified Geometry

Finite element analysis was employed to verify if the above specimen configuration is an accurate simulator of actual die attach constraints. A three-dimensional (3-D) finite

element model was developed using ANSYS® as shown in Figure 3.2. The model of the die attach was subject to normal (tensile) and shear loading.

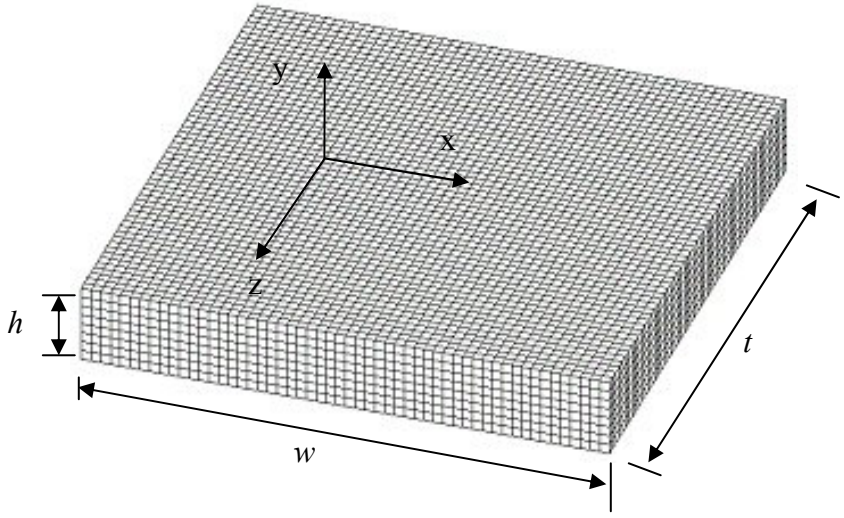

Fig. 3.2

3-D Finite element Model of die attach shown for t/w=1

{t – thickness (depth), w – width, h – height}

The model was solved for different t/w aspect ratios (keeping the width constant) to ascertain whether the specimen with a t/w of 0.75 could accurately represent the die attach. The above figure is shown for an aspect ratio of 1 (t/w=1). To assess the effect of die attach thickness (depth), stresses at center point in mid-plane were plotted for different values of thickness. When t/w = 2.5, all stresses started to saturate and there was no apparent stress difference for t/w greater than 2.5. Maximum stress difference for σ_x was less than 2.2%. Maximum stress difference for σ_y was less than 0.9%. However, maximum stress difference for σ_z was more than 130% and appeared to be largely affected by thickness. Such a large percent difference is misleading because σ_z was found to be negligibly smaller in magnitude as compared to other stress

components. Maximum stress difference for τ_{xy} was less than 0.06% and also negligible. As observed from Figures 3.3, 3.4, 3.5, and 3.6, between two cases of t/w=1 and t/w=0.75, the stress differences were 0.7%, 0.3%, 51% and 0% for σ_x, σ_y, σ_z, and τ_{xy}, respectively. The dotted circles denote stress differences for aspect ratios 0.75 and 1.

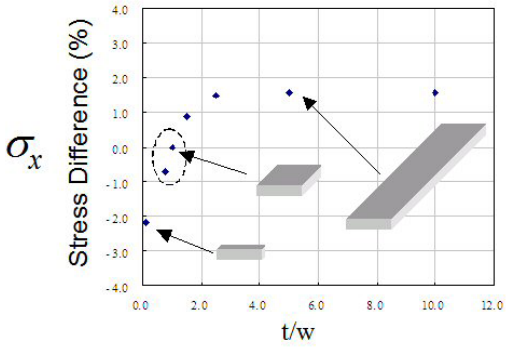

Fig. 3.3

σ_x plotted as function of aspect ratio

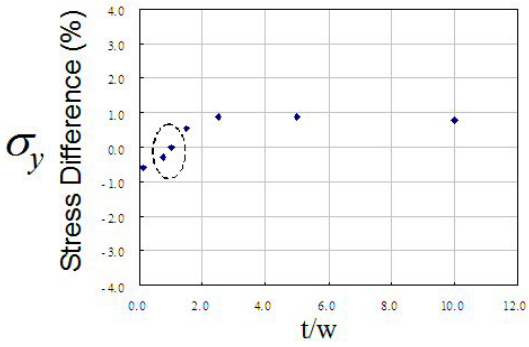

Fig. 3.4

σ_y plotted as function of aspect ratio

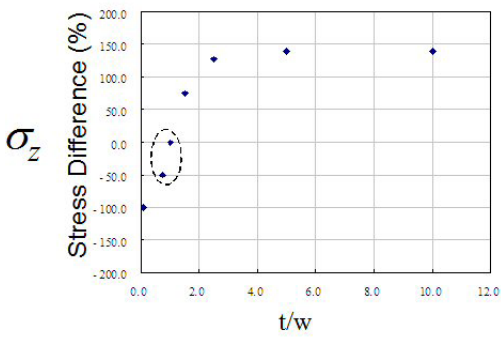

Fig. 3.5

σ_z plotted as function of aspect ratio

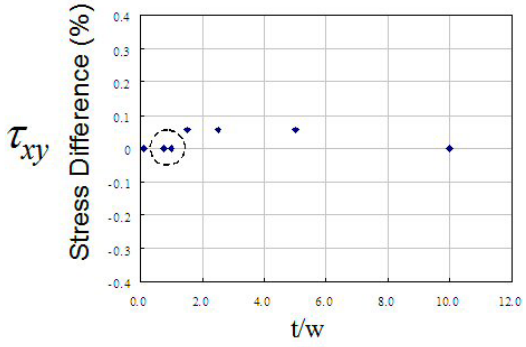

Fig. 3.6

τ_{xy} plotted as function of aspect ratio

As mentioned earlier, the effects of σ_z were neglected despite the large percent stress difference for the two aspect ratios. The stress differences for the remaining three stresses were also negligible, and one could safely conclude that because shear stress

was the dominant mode of deformation, a specimen with an aspect ratio of 0.75 (t/w=0.75) could simulate the constraints in the actual die attach (t/w=1) with minimal effect of change in thickness. If the thickness of solder specimen was increased from t/w=0.75 to t/w=1, it could better simulate actual die attach constraints, however, the specimen preparation and testing method would become more complicated. Hence t/w=0.75 was maintained throughout the program.

Increasing or decreasing the height of the solder joint may affect the stress/strain fields and subsequently the mechanical properties of the material, e.g. the relative grain size and the intermetallic layer will have a pronounced effect when joint height is reduced to the scale comparable to the grain size of solder. It should be noted that this analysis did not consider the solder joint height since the height used (100μm) was on the same scale as that of a die attach used in actual assemblies.

However, before the specimen with the new joint height of 100μm could be used for testing, several alterations were required to be made to the specimen preparation procedure explained in Section 2.2. These changes are described in detail in Section 3.2 below.

3.2 Modification of Specimen Preparation Procedure for the 95.5Pb2Sn2.5Ag solder alloy

The material properties of the solder joint depend on its microstructure. A stable and

consistent microstructure significantly improves the repeatability of experimental data. The microstructure of the joint depends on its size and the reflow temperature profile. An optimum reflow temperature profile can be developed with the accurate knowledge of the phase transition temperatures of the solder alloy. The solder material in this study is the high temperature, high lead 95.5Pb2Sn2.5Ag solder with a joint height of 100μm. Thus, suitable modifications must be made to obtain specimens with a stable and consistent microstructure.

3.2.1 Preparation Procedure

The copper platens were initially manufactured at the Physics Machine Shop at the University of Maryland, College Park. However, later it was decided to prepare the platens at Infineon Technologies AG using *Wieland® K80* copper, first electroplated with nickel (depth - 1μm), then chemically (electroless) plated with Ni-P (depth - 3μm). This simulated the process followed by Infineon Technologies AG for soldering the chip to the substrate in high power devices. It is known that at the Cu/solder interface, Sn reacts rapidly with Cu to form a Cu-Sn intermetallic compound (IMC), which weakens the solder joint due to the brittle nature of the IMC. The strength of the solder joint decreases with the increasing thickness of the IMC formed at the interface and the IMC acts as initiation sites for micro-cracks [Alom et al., 2002]. The electroless Ni-P plating improves the interface properties. Studies have shown that that a Ni/solder interface has a much slower IMC growth rate as compared to a Cu/solder interface. Ni thus acts a diffusion barrier between Cu and the solder in order to sustain a longer period of service [Chan, et. al., 1998]. The effect of

the interactions at the Cu/solder interface is not accounted for in this study and is beyond the scope of this thesis.

The basic requirements in producing quality specimens are cleanliness of active (eventually soldered) surfaces and precise alignment of the two platens used. To this end, the active surfaces were first cleared of contaminants by smoothing with a medium fine grade (1000-A) sand paper and then rinsed thoroughly with IPA to remove any remaining debris.

A special-purpose soldering fixture was designed for reflowing the solder joint. Dowel pins were used for locating the platens on the fixture such that the two active surfaces are precisely aligned. Figure 3.7 shows the modified soldering fixture used for reflow soldering. Since the gauge diameter of the wire used as raw material is 800μm, small pieces of the wire had to be cut, twisted into a braid and flattened as far as possible to fit it in the 100μm gap between the two copper platens. Steel shims were wedged between the platens to maintain a joint height of 100μm. The platens were held tightly in place by a screw driven plate, which also helps maintain the two platens parallel to each other during reflow.

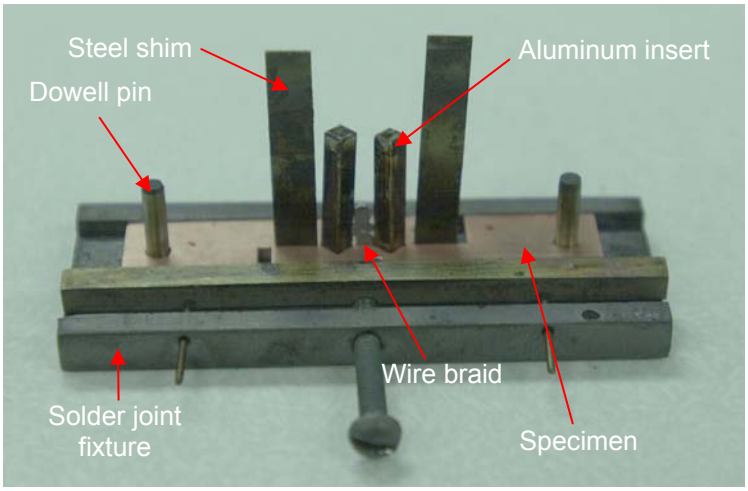

Fig. 3.7

Soldering Fixture

It was essential to control the actual solder joint dimensions as close to the nominal dimensions as possible to avoid variations in experimental data due to erroneous estimation of stress and strain. Silicone rubber could be used for preventing the flow of solder down the slope of the V-notch during reflow soldering at temperatures above 260^{o}C, since Dow Corning® heat resistant sealant No.736 has a maximum usable temperature of approximately 260^{o}C for intermittent exposure. It was decided that an insert acting as a plug, fitting the V-notched square gap at either side of the eventual solder joint, be used for the purpose rather than the silicone rubber.

A cheap, easily available and easily fabricated material, namely, aluminum was chosen as the material for the insert. Aluminum has a high melting point (660^{o}C) and is not wetted by solder. The silicone rubber has a curing time of 12 hours. Thus, using aluminum inserts not only helped control solder joint width, but also helped to significantly reduce the specimen preparation time, since curing time was saved.

The reflow profile used had five main parameters:

- Preheating time
- Preheating temperature
- Peak temperature
- Dwell time at peak temperature
- Cooling rate

And consisted of the three heating stages:

- Preheating
- Flux activation hold
- Spike and reflow

The preheating temperature needed to be set to permit sufficient time to activate the flux. The flux used in this study was a rosin-based mildly activated flux (Kester #186 type RMA – 61% 2-Propanol, 39% Rosin), which was specified for activation between 130^{o}C and 150^{o}C. The wrong preheating profile could cause insufficient fluxing or decomposition of the organic flux. The third stage was to spike the temperature quickly to the peak reflow temperature (usually 1-2^{o}C/s) to avoid charring or overdrying of the organic flux. Peak temperatures used are generally 25-50^{o}C higher than the liquidus temperature of a particular solder alloy, for example, the typical peak temperature for SnPb eutectic solder is 233^{o}C for a liquidus temperature of 183^{o}C.

Another important parameter is dwell time at peak temperature. The wetting ability is directly related to the dwell time at peak temperature. Peak temperature and dwell time were set to obtain an optimum balance between good wetting, minimal void formation and low intermetallic compound formation. The dwell time was short enough to minimize intermetallic formation, while being long enough to achieve good wetting and to expunge any non-solder (organic) ingredients from the molten solder before it solidified, to minimize void formation [Hwang, 1996].

The liquidus temperature of the 95.5Pb2Sn2.5Ag solder is 304^{o}C. Reflow soldering was conducted at a peak temperature of 380^{o}C in an effort to simulate the peak temperature encountered by assemblies during reflow at Infineon Technologies AG. Figure 3.8 shows the schematic of the reflow temperature profile for the 95.5Pb2Sn2.5Ag solder alloy, and Figure 3.9 shows the actual reflow profile used. As can be seen, flux activation was carried out at 130^{o}C and reflow at 380^{o}C. The specimen was cooled down to room temperature by setting it on a thick aluminum cold plate used as a heat sink. Optimum parameters for reflow were established using the above guidelines, as well as engineering judgment and experience. Figure 3.10 shows the typical solder joint under the optical microscope.

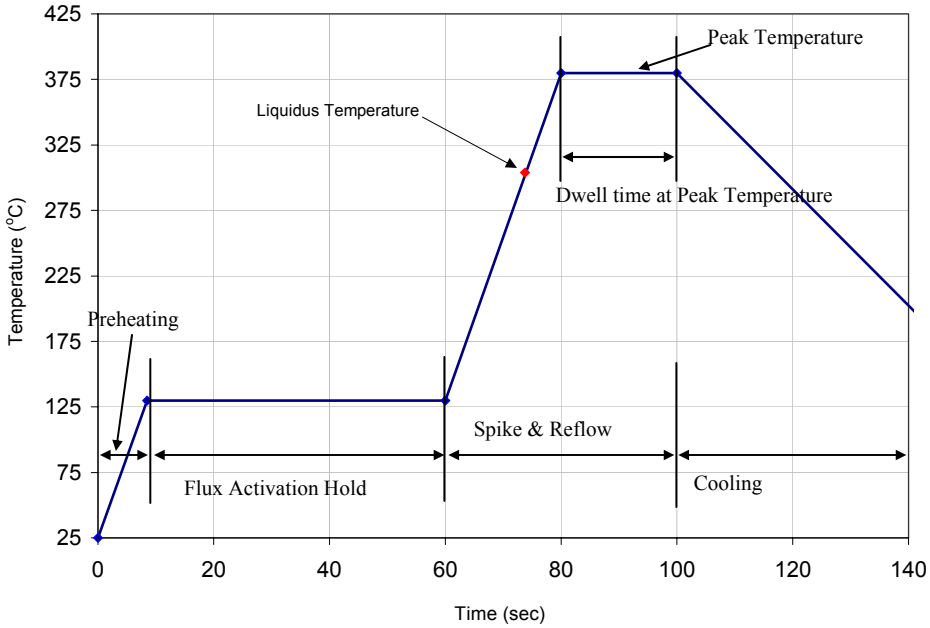

Fig. 3.8

Schematic of Reflow Temperature Profile for 95.5Pb2Sn2.5Ag solder

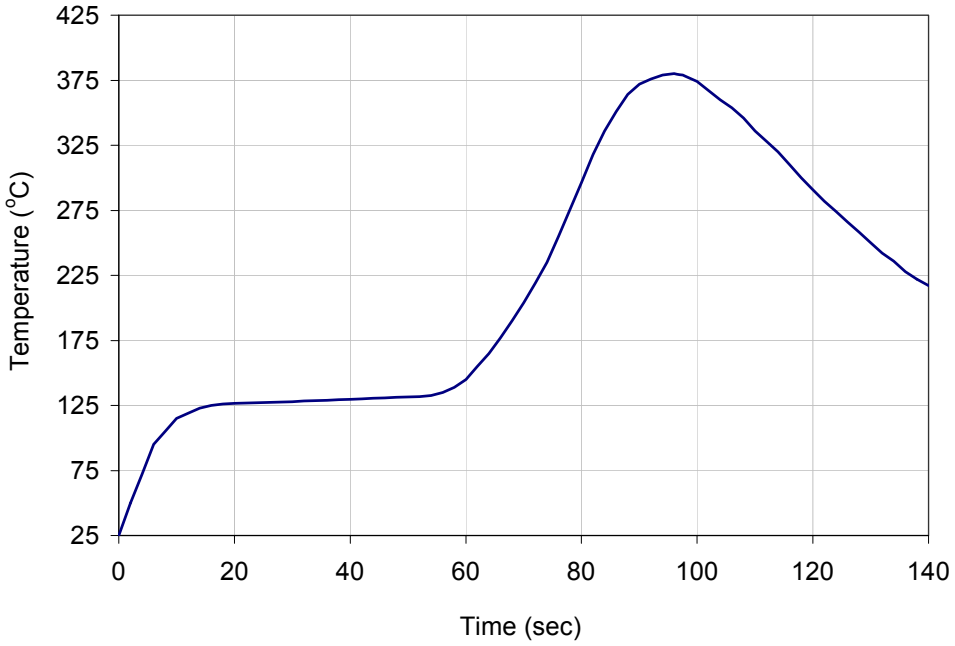

Fig. 3.9

Actual Reflow Temperature Profile for 95.5Pb2Sn2.5Ag solder

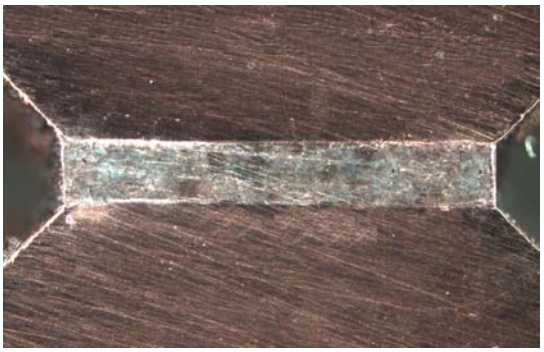

Fig. 3.10

Typical solder joint as viewed under optical microscope

There were a few key issues during specimen preparation, which if ignored could have resulted in poor specimen quality:

- *Improper location on fixture*- caused specimen misalignment leading to stress-related damage during subsequent steps.
- *Improper cleaning and flux activation*- caused poor joint quality, e.g. voiding or poor wetting of solder to copper.
- *Flowing of solder along the Iosipescu grooves*- caused joint dimensions to deviate from the nominal dimensions leading to erroneous stress-strain calculations.
- *Incorrect reflow temperature profile*- caused variations in joint microstructure and hence variation in measurements.
- *Stressed joint during polishing and pin press fitting*- caused interfacial cracks and delamination of the joint, which shifted the failure mechanism from the bulk of the solder joint to the Cu/solder interface. This was usually manifested as a sudden load drop in the load-displacement curve.

Figures 3.11 to 3.22 give an idea of the specimen preparation process concerns. Errors were separated into four major categories:

- Misalignment of copper platens
- Poor width control
- Poor Wetting
- Voiding

Each error source was isolated and corrected one at a time.

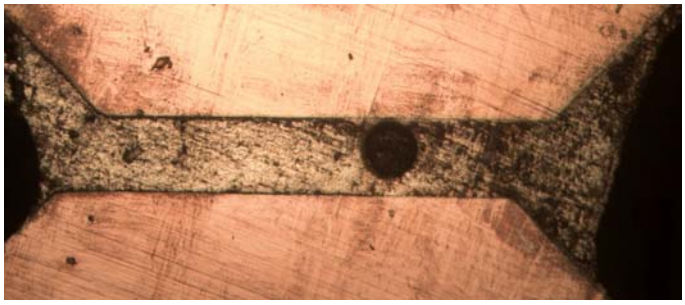

Fig. 3.11

Early specimen: Misalignment, voiding, poor width control

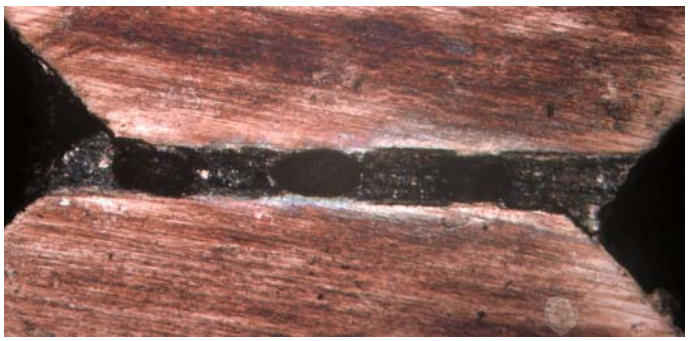

Fig. 3.12

Early specimen: Severe Misalignment and Voiding

(Designed new reflow fixture)

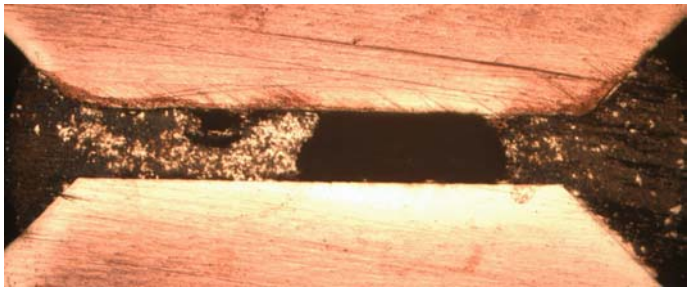

Fig. 3.13

Void and poor width control

(Designed Aluminum inserts for width control)

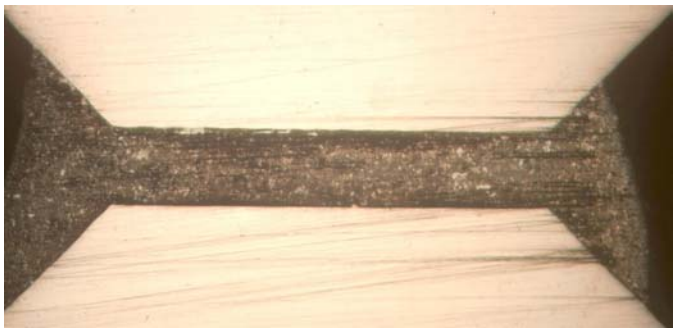

Fig.3.14

Poor width control

(Designed new reflow fixture)

Fig.3.15

Voiding

(Varied flux amount, preheat time, and dwell time at peak temperature)

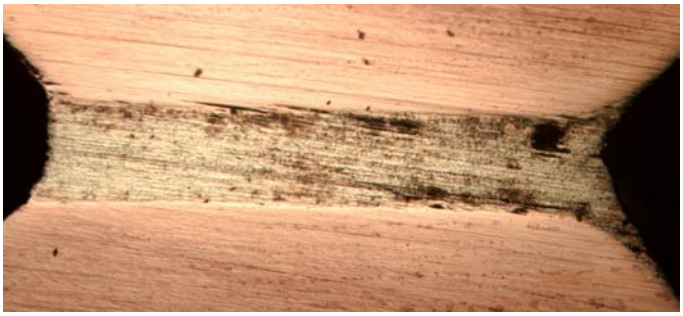

Fig. 3.16

Voiding

(Varied flux amount, preheat time, and dwell time at peak temperature)

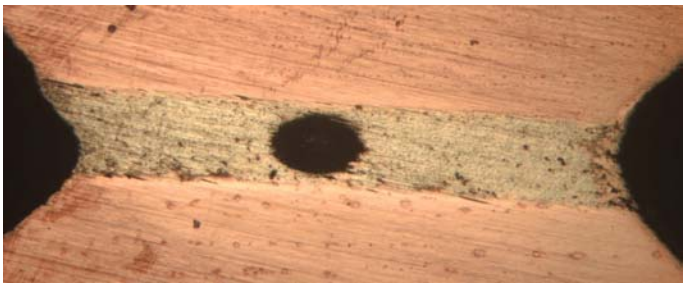

Fig. 3.17

Voiding

(Varied flux amount, preheat time, and dwell time at peak temperature)

Fig. 3.18

Voiding

(Varied flux amount, preheat time, and dwell time at peak temperature)

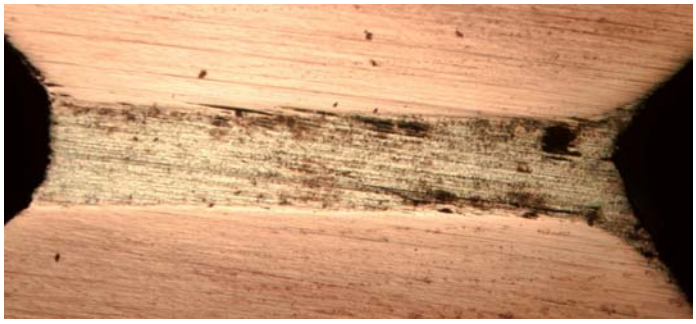

Fig. 3.19

Voiding

(Varied flux amount, preheat time, and dwell time at peak temperature)

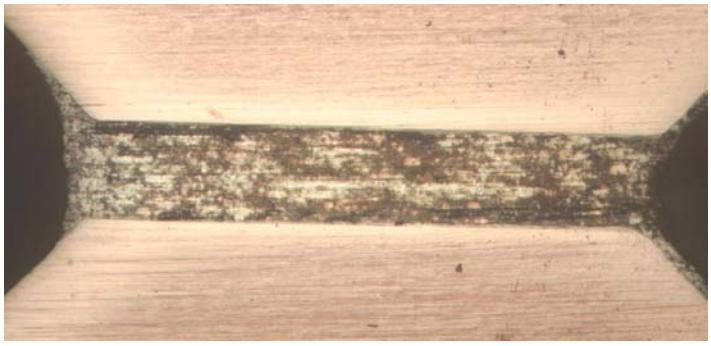

Fig. 3.20

Good solder joint quality

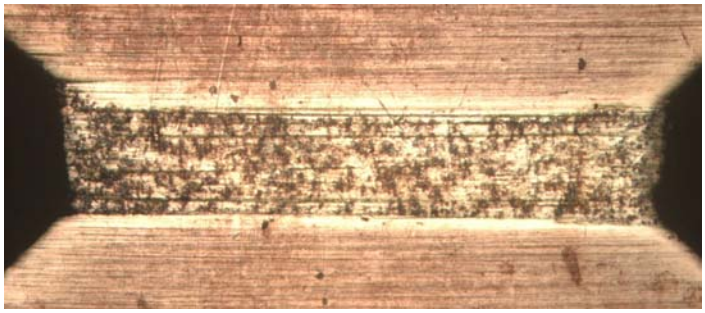

Fig. 3.21

Good solder joint quality

Fig. 3.22

Good solder joint quality

3.2.2 Specimen Quality Verification

Visual inspection was used to screen specimens with surface defects such as voids or cracks. However, sub-surface defects significantly contribute to the scatter in experimental data. To improve repeatability of test data, quality assurance was conducted through common non-destructive and destructive evaluation techniques, which are described below.

3.2.2.1 Non-destructive Testing

Non-destructive testing techniques were the preferred method of quality assurance simply because the specimen condition was not altered and if found acceptable, was usable for experimental purposes after the evaluation. The most common method of non-destructive evaluation in electronics packaging is acoustic microscopy. A Sonix® Scanning acoustic microscope (SAM) was used to screen specimens with subsurface voids.

In acoustic microscopy, a piezoelectric transducer emits and scans ultrasonic pulses of energy across the surface of a part, which is immersed in a water bath. The ultrasonic beam is focused using lenses within the part. The image resulting from these scans is termed a C-Scan. Scanning Acoustic Microscopes have two distinct operating modes, from which images can be generated, namely *pulse echo* and *through-transmission*.

The pulse echo mode is a single sided technique using one transducer to send a pulse out and receive the return echo from the part under testing. Amplitude, phase change and the depth information can be extracted from the generated acoustic signal. When the acoustic wave travels from a material with high acoustic impedance (solder) to a material with low acoustic impedance (air), a reflected signal's phase is inverted. This is a possible indication of presence of voids.

Through transmission is a dual sided technique that uses two transducers, one on the front to send the ultrasonic pulse and the other on the backside to receive it. This mode works best for a quick check for voids within packages. In the transmission mode, black areas indicate a low amount of transmission and white areas indicate very high transmission. Thus, voids will show up as black spots as they reflect sound and thereby prevent transmission to the receiving transducer.

A 15MHz low frequency transducer was used in Pulse echo and through transmission modes to check for subsurface voids in the solder joint. The transducer was able to

detect a difference in the acoustic impedance when the sound wave hit a void inside the solder joint. Acoustic impedance is given by:

$$Z = \rho c \tag{3.1}$$

where ρ is the density of the medium, and c is the velocity of sound in that medium. Fig. 3.23 and 3.24 are provided as illustrative examples of specimens with voids and no voids.

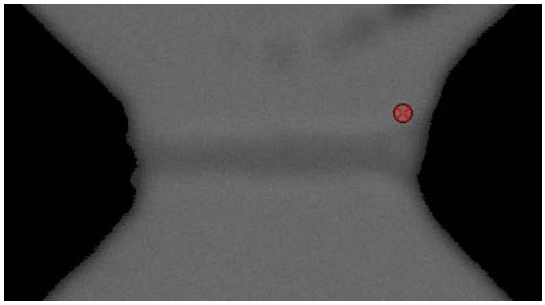

Fig. 3.23

C-Scan of a specimen with SAM (no void)

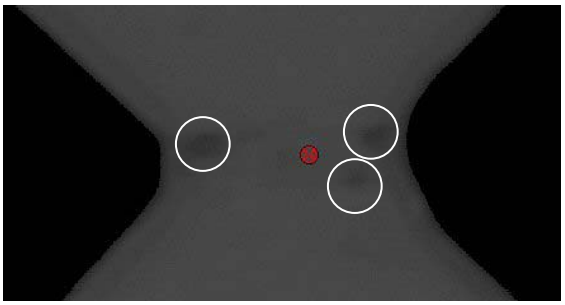

Fig. 3.24

C-Scan of a specimen with SAM (voids)

3.2.2.2 Destructive Testing

The SAM with a 15MHz transducer has a resolution of 50μm, i.e. it cannot detect voids with diameter less than 50μm. Therefore for quality assurance, two specimens were randomly selected from every batch of ten specimens, for cross sectioning. The specimens were potted in an epoxy compound with 10:3 resin:hardener ratio. The encapsulation was done to have support for the fragile solder joint while cross sectioning them. After the epoxy was cured, excess molding compound was ground off using a coarse 240 grade sand paper. Subsequent grinding was conducted in stages, with decreasing grit size (400, 600, 700, and 1200) of waterproof metallurgical SiC sandpaper. A final polish was done using 0.3μm Al_2O_3 powder, 0.05μm Al_2O_3 powder, and finally 0.05μm silica. The solder joint was inspected for voids or delamination, at every 20μm, each time after final polish. Cross-sectioned images are shown below in Figures 3.25, 3.26 and 3.27 for illustration of a specimen with and without voids of acceptable size.

Fig. 3.25

Cross sectioned specimen (early specimen)

(Unacceptable-batch not used for testing)

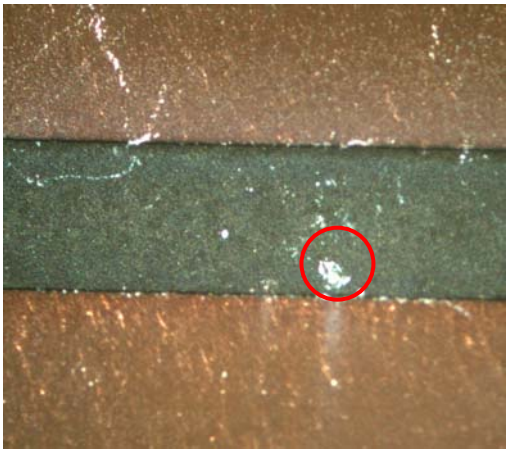

Fig. 3.26

Cross sectioned specimen (Acceptable)

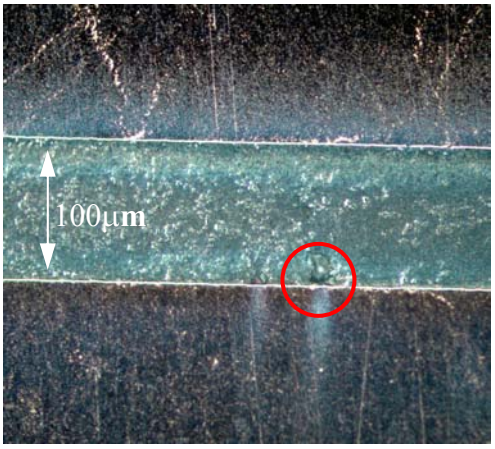

Fig. 3.27

Cross sectioned specimen (Acceptable)

The batch was deemed fit for testing, if the total void volume fraction for each specimen was less 5% of the total solder joint volume. All voids were assumed to be spherical. The diameter of the voids was measured using an optical microscope.

3.3 Experimental Set-up

As mentioned in section 2.4, difficulties arise in making measurements with using a miniature specimen for testing. A novel technique for direct local measurement of strain using a miniature axial extensometer developed by Kwon et al. [2003] has been employed for the strain measurements of 95.5Pb2.Sn2.5Ag solder single-lap shear specimens. Figure 3.28 shows the experimental set-up.

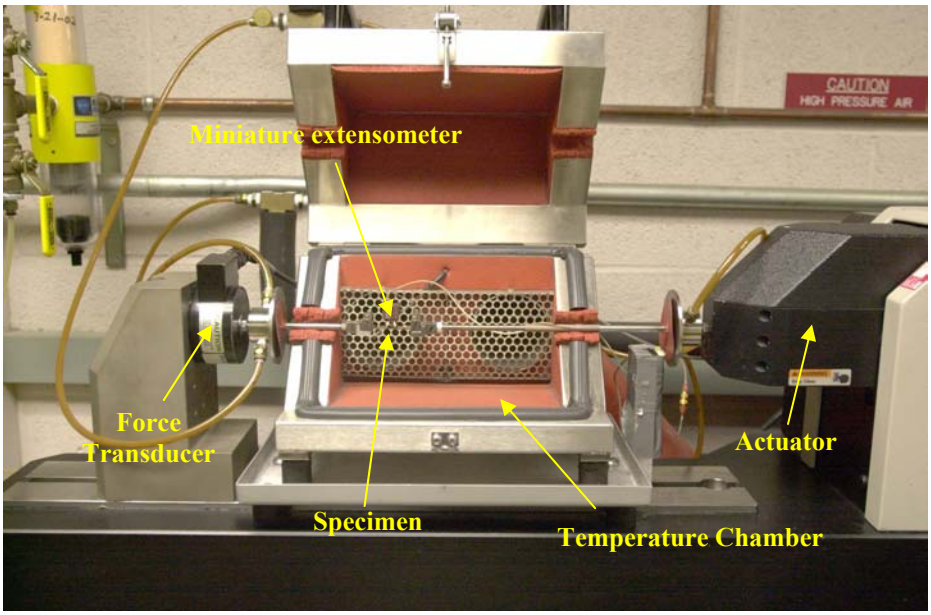

Fig. 3.28
Experimental Test Set-up for MTS Tytron™ Testing System

This direct local measurement technique involved the use of a high resolution MTS 632.29F-20 miniature axial extensometer for making strain measurements. This extensometer had two knife-edges with a gauge length of 3mm, and was attached to the specimen by means of elastic bands with a force of approximately 400gm. In

order to accurately measure the deformation of the solder, it was decided that the extensometer be mounted atop an extended structure, which would consist of two *extensions*, each fixed on top of one of the two copper platens of the specimen. For this purpose, a hole was provided on each copper platen, into which after polishing the specimen, a steel pin was press fitted. The extensions could then be slid onto the pins extending from the specimen and attached to these pins with room temperature curing high temperature epoxy adhesive taking care that they do not come in contact with the specimen below. Figure 3.29 shows the extensions fixed on top of the specimen with the extensometer attached above.

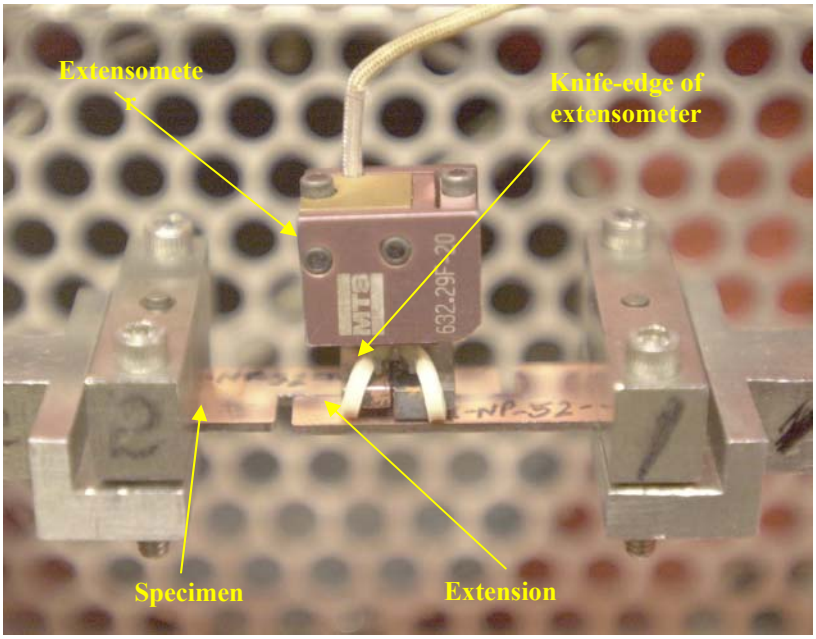

Fig. 3.29

Close-up view of specimen mounted on machine

3.4 Subtracting the Compliance Effects of Copper

Section 2.5 explains the methodology devised by Kwon et al. [2003] for subtracting the effects of compliance of copper on the measurement of solder deformation. The same methodology has been adapted in this study for the specimen with a nominal joint height of 100μm as opposed to that of 300μm used by Kwon et al. [2003]. Certain aspects of the method described in Section 2.5 have been repeated here for the sake of continuity.

Finite element analysis (FEA) was used to subtract the compliance effects of copper from the measured deformation. The FEA tool ANSYS® was employed to simulate the deformation of the specimen under the application of an arbitrary force. A linear, isotropic, structure using PLANE82, a two-dimensional (2-D) plane stress, 8-node element was used to model the geometry of the specimen. The mesh used for analysis is shown in Figure 3.30a. Figure 3.30b shows the deformed state with highly exaggerated deformation.

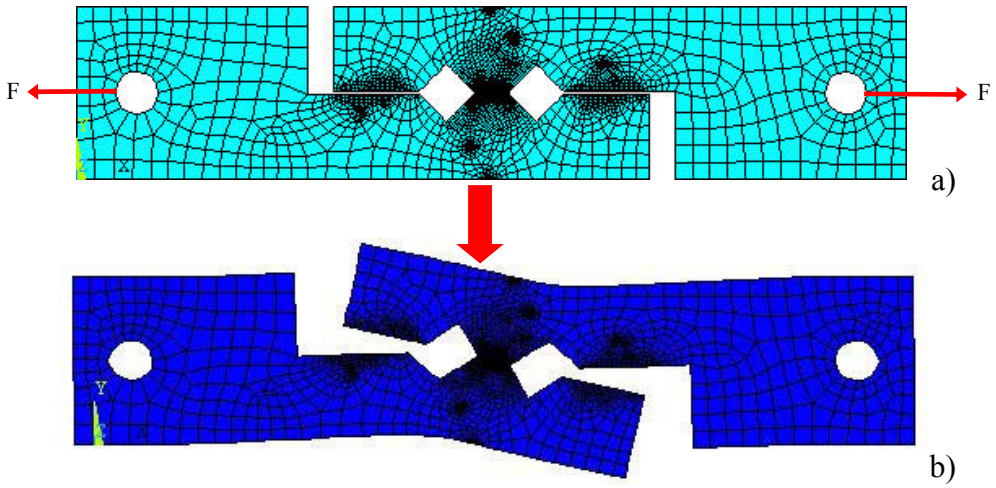

Fig. 3.30

a) Finite Element Mesh generated for lap shear specimen,

b) Deformed state (exaggerated) when an arbitrary force is applied to the specimen

This element type provides more accurate results for mixed (quadrilateral-triangular) automatic meshes and can tolerate irregular shapes without as much loss of accuracy. The 8-node element is defined by eight nodes having two degrees of freedom at each node, viz. translations in the nodal x and y directions. The material properties used for this evaluation are shown in Table 3.1. All materials were assumed to be elastic in nature.

Material	**Elastic Modulus (Pa)**	**Poisson's Ratio**
Copper (Cu)	10.4×10^{10}	0.35
Steel (Fe)	19.3×10^{10}	0.25
Lead (Pb)	1.38×10^{10}	0.4

Table 3.1: Input properties of materials used in FEA

Mesh convergence was carried out for the model to make sure that the results are independent of the mesh. The maximum shear stress value, averaged over 8 elements at the center point in mid-plane of the solder joint, was used as the mesh convergence criteria. The mesh was refined until the value of the maximum shear stress reached a saturation point. The mesh convergence plot for the model is shown in Figure 3.31. The results presented are for the mesh with 4650 elements.

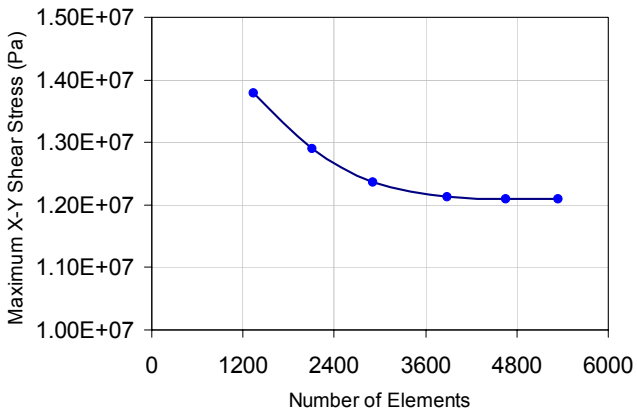

Fig. 3.31

Mesh Convergence plot

Using Equations (2.1) to (2.6) from Section 2.5, all the required parameters and correction factors can be calculated for a particular specimen thickness. The finite element model was solved for different values of thickness, and a plot of compensation rate as a function of the specimen thickness was obtained as shown in Figure 3.32.

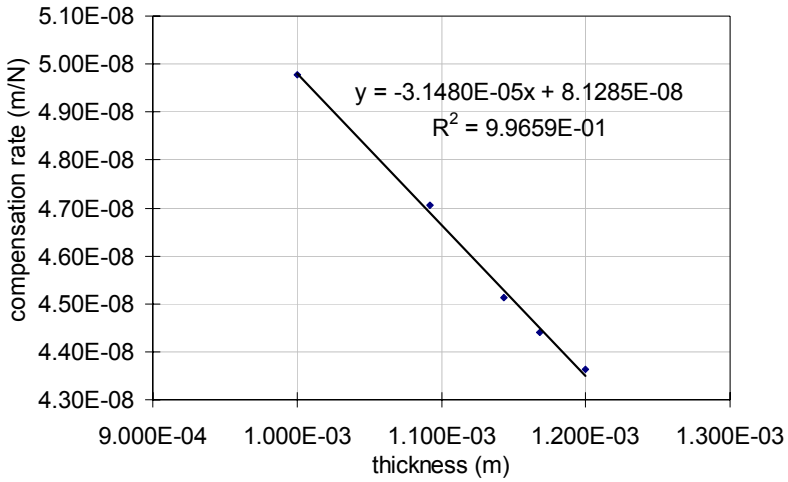

Fig. 3.32

Compensation Rate Curve obtained via FEA

This plot served as a quick calculator of the compliance effects of the copper on the deformation of the solder joint, for any specimen thickness, and could be immediately subtracted to obtain shear deformation of solder. Figure 3.33 demonstrates the effect of copper compliance on the deformation measurement of the solder joint. It was evident that the effect of copper compliance was tangible only in the elastic and plastic regions of the stress strain curve and was negligible once the strain hardening is nearly zero and the plastic flow reaches a steady state of balance between strain hardening and stress relaxation. Thus the compliance of copper had minimal effect on the creep properties of the solder joint.

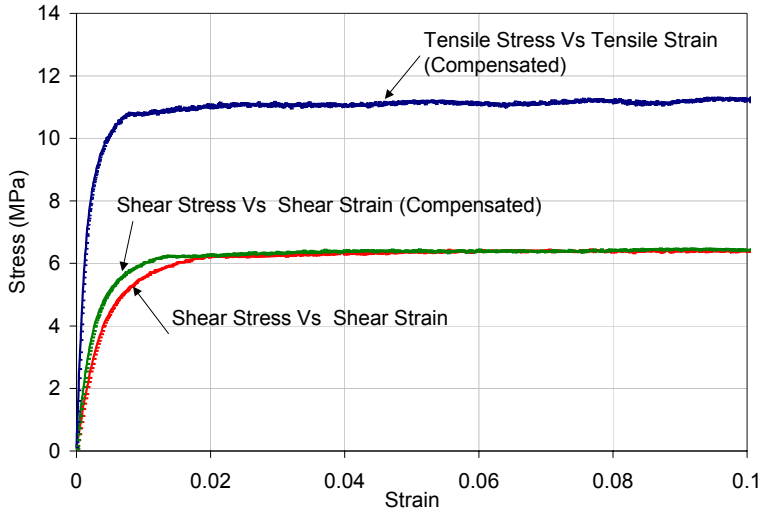

Fig. 3.33

Effect of compliance compensation on typical Stress strain curve

In summary, implementation of the DLMT for 95.5Pb2Sn2.5Ag solder die attach involved several modifications, including solder joint geometry and preparation procedure. The nominal specimen dimensions were changed to simulate geometric and loading constraints in a large area die attach. The specimen preparation procedure was modified on the basis of solder joint height, phase transition temperature and void formation. A new fixture was designed to minimize specimen misalignment errors in the load-displacement curve. Numerical analysis was used to derive a new compensation rate curve to account for the effects of copper compliance on measurement of solder deformation for a joint height of 100μm.

The test matrix and the constitutive properties obtained for the 95.5Pb2Sn2.5Ag solder die attach by implementing the DLMT are presented in Chapter 4.

Chapter 4. Constitutive Properties of 95.5Pb2Sn2.5Ag solder

4.1 Introduction

Monotonic, isothermal tests were conducted on 95.5Pb2Sn2.5Ag solder at constant (shear) actual strain rates from $1x10^{-2}s^{-1}$ to $1x10^{-6}s^{-1}$ over a temperature range from $25^{o}C$ to $150^{o}C$ (0.5 to 0.75 homologous temperature) in strain control, to study the effects of strain rate and temperature on the mechanical properties in a systematic manner. The test matrix used in this study is shown in Figure 4.1 below:

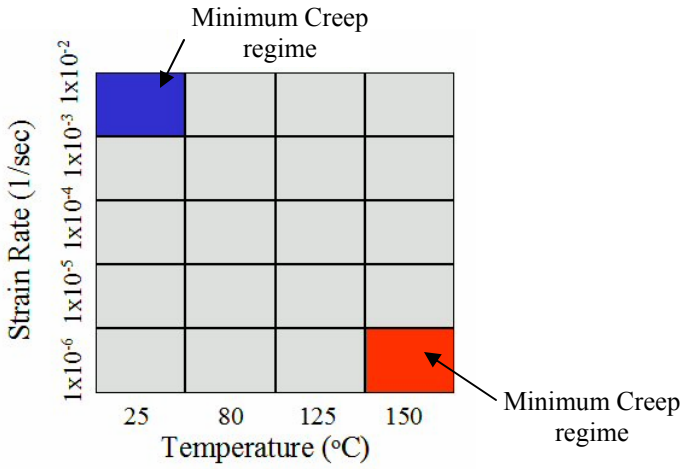

Fig. 4.1

Test Matrix

The chosen solder alloy has a melting point of $304^{o}C$, however, the highest possible temperature with the current configuration was $150^{o}C$, which permitted experimentation at a maximum of 0.75 homologous temperature to obtain the constitutive properties. The material characterized is highly compliant and the range

of strain rates chosen ($1x10^{-2}s^{-1}$ to $1x10^{-6}s^{-1}$) was considered to be wide enough to obtain time-independent plastic and time-dependent creep deformation. The stress-strain behavior obtained at these temperatures and strain rates is plotted in Figures 4.2 through 4.5.

The flow stresses at corresponding strains were observed to be strong functions of strain rate, with the stresses increasing with the strain rate due to less time for thermally activated processes. Since thermally activated processes occurred faster at higher temperatures, the stresses at corresponding strains were progressively lower at 150°C as compared to 25°C.

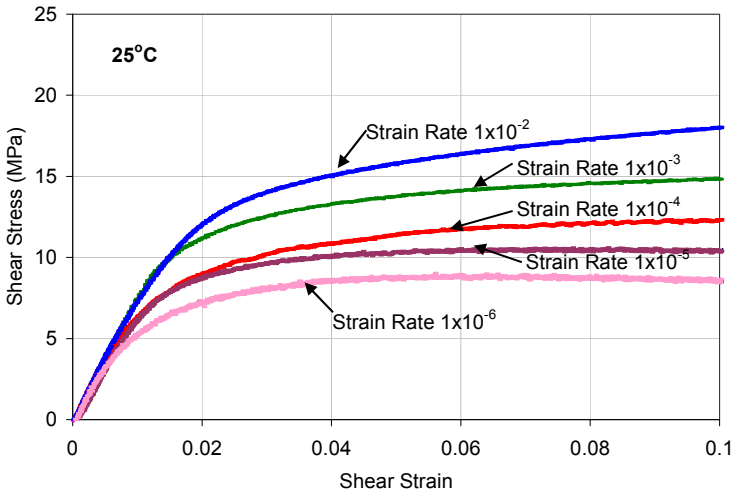

Fig. 4.2

Stress-strain curves at 25°C

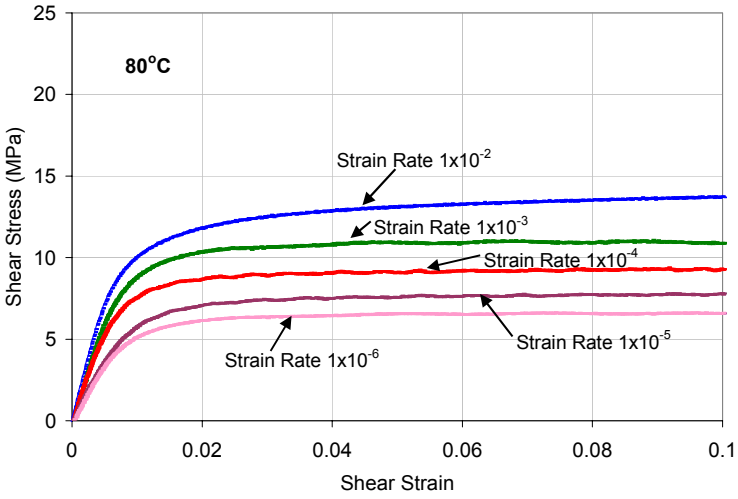

Fig. 4.3

Stress-strain curves at 80°C

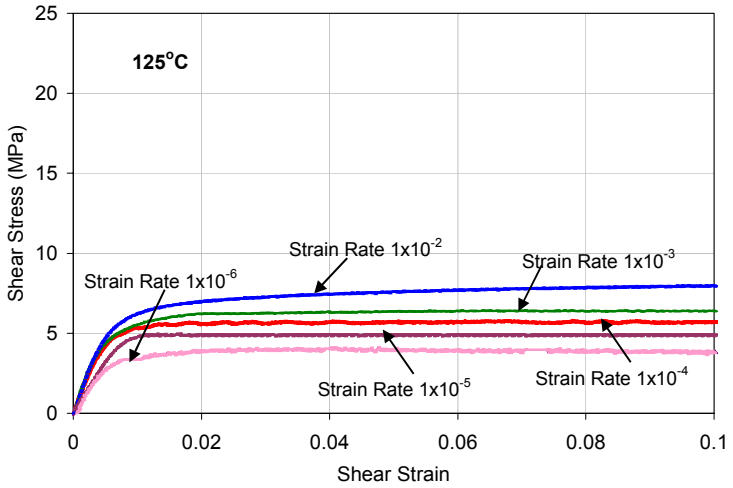

Fig. 4.4

Stress-strain curves at 125°C

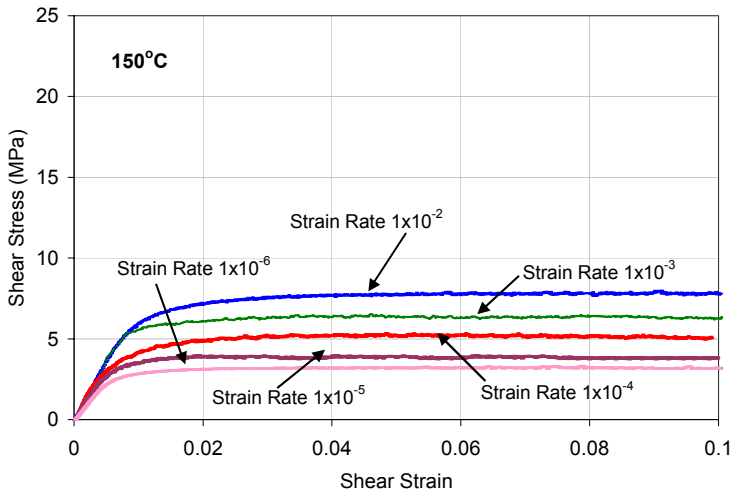

Fig. 4.5

Stress-strain curves at 150°C

Using the above stress-strain curves, the dependencies of yield stress and ultimate tensile strength on temperature and strain rate were obtained in addition to the partitioned constitutive property measurements for the 95.5Pb2Sn2.5Ag solder alloy.

4.2 Yield Stress and Ultimate Tensile Strength

Yield stress and Ultimate tensile strength (UTS) were found to decrease with temperature and increase with strain rate. Shi et al. [1999] made similar extrapolations from their investigations with 63Sn/37Pb eutectic solder. Figures 4.6 and 4.7 show the dependency of yield stress on temperature and strain rate, and figures 4.8 and 4.9 show the dependencies for ultimate tensile strength of 95.5Pb2Sn2.5Ag solder. The values for Yield stress obtained through testing are shown in Table 4.1. The stress at 0.2% strain was taken as yield stress.

Strain Rate (1/sec)	Yield Stress (MPa)			
	25°C	**80°C**	**125°C**	**150°C**
$1x10^{-2}$	20.8	16.8	13.8	1.1
$1x10^{-3}$	18.7	15.3	11.8	9.6
$1x10^{-4}$	16.3	12.9	9.4	7.2
$1x10^{-5}$	13.5	10.8	7.9	5.5
$1x10^{-6}$	11.1	8.3	5.8	4.0

Table 4.1: Yield stress for 95.5Pb2Sn2.5Ag

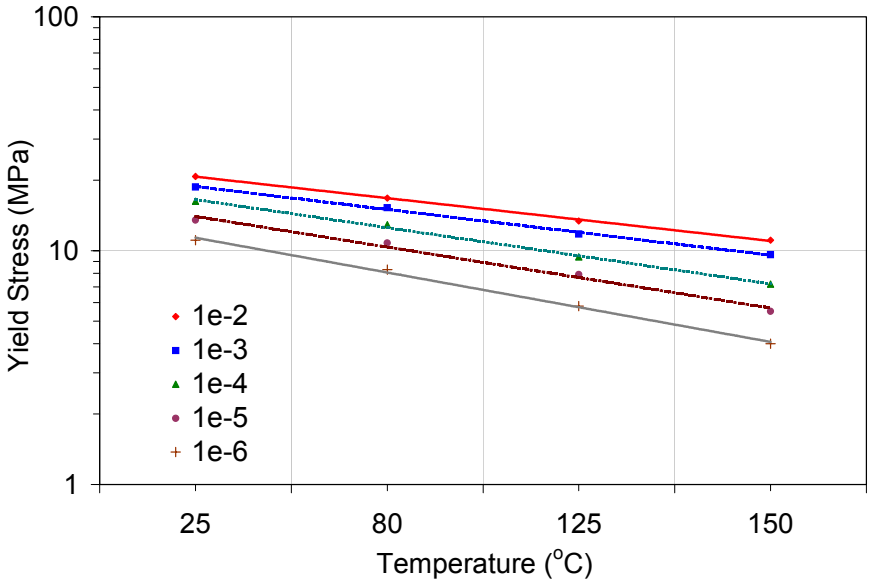

Fig. 4.6

Yield Stress of 95.5Pb2Sn2.5Ag as a function of temperature

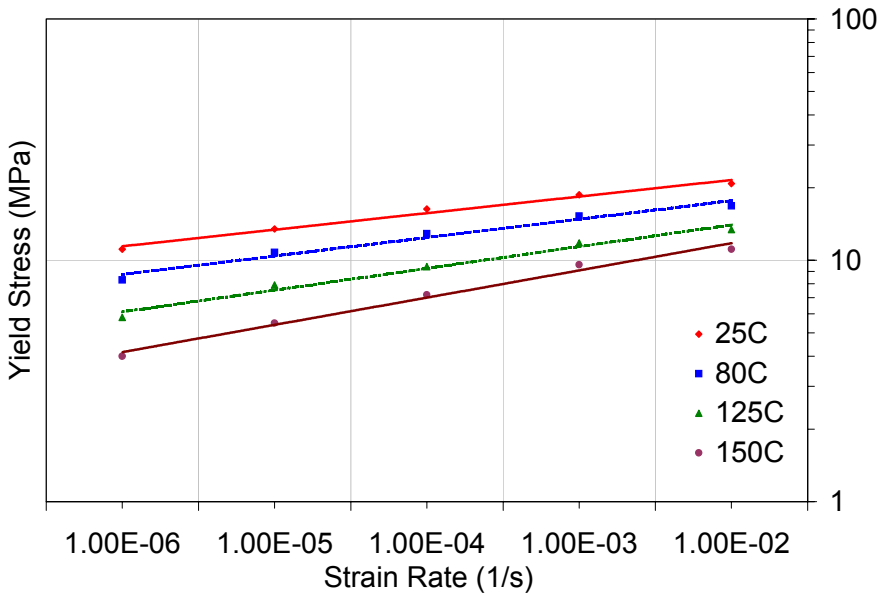

Fig. 4.7

Yield Stress of 95.5Pb2Sn2.5Ag as a function of strain rate

The above plots demonstrated that there was an approximately linear relationship between the yield stress and temperature. However, it was evident that the yield stress increased with strain rate in a non-linear manner. Two trends were visible. The slope of each curve was slightly different at each temperature and increased with am increase in temperature. The curve at 25^{o}C was almost linear on the log-log plot and became increasingly non-linear as test temperature was increased to 150^{o}C. The other trend was that the higher the temperature and the lower the strain rate, the greater was the variation in yield stress. This was attributed to the fact that creep deformation makes a larger contribution to the reduction in strength at higher temperatures and lower strain rates.

The values obtained for UTS are shown in Table 4.2 below. The value corresponding to the maximum stress in the stress-strain curve was taken as the UTS.

Strain Rate (1/sec)	Ultimate Tensile Strength (MPa)			
	25°C	**80°C**	**125°C**	**150°C**
$1x10^{-2}$	33.1	25.6	16.6	13.3
$1x10^{-3}$	28.3	20.6	13.3	10.9
$1x10^{-4}$	23.9	16.9	10.9	9.0
$1x10^{-5}$	19.4	13.6	8.8	6.8
$1x10^{-6}$	15.7	10.7	6.4	4.7

Table 4.2: Ultimate Tensile Strength for 95.5Pb2Sn2.5Ag

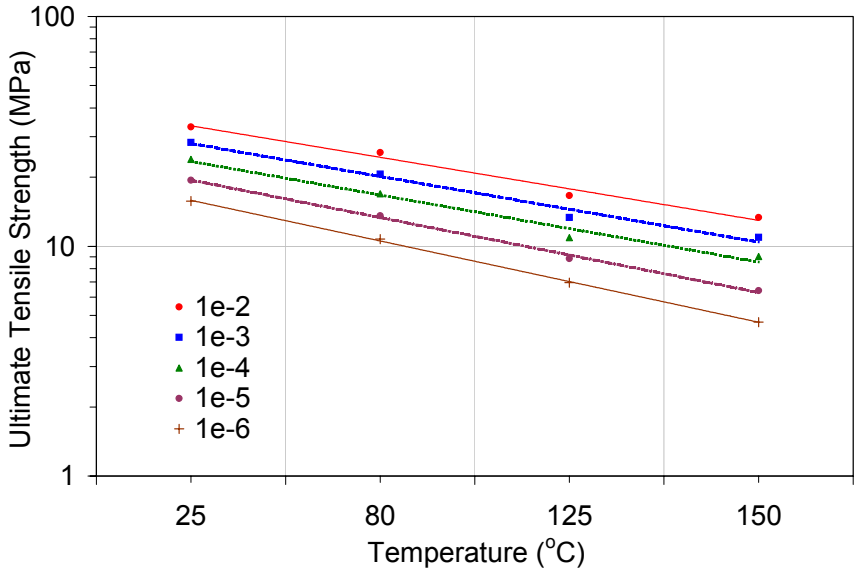

Fig. 4.8

Ultimate Tensile Strength of 95.5Pb2Sn2.5Ag as a function of temperature

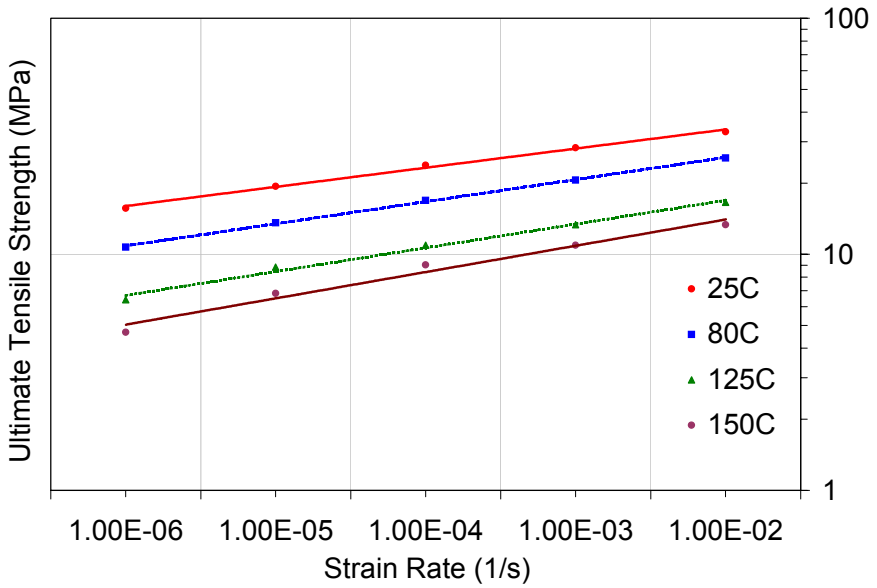

Fig. 4.9

Ultimate Tensile Strength of 95.5Pb2Sn2.5Ag as a function of strain rate

The UTS showed an approximately linear relationship with temperature just as in the case of yield stress. UTS also demonstrated a fairly linear relationship with strain rate at lower temperatures, but the trend suggested a non-linear relationship at higher temperatures and lower stain rates. A clearer picture may be obtained with tests conducted at $T>0.8T_m$ and $1x10^{-7}$ to $1x10^{-9}$ strain rates. This observation again however, seemed to suggest creep deformation to be dominant at lower strain rates and higher temperatures.

4.3 Time-independent Elasticity

The shear modulus of the solder alloy was determined by a combination of two methods.

Method I

In the first method, 10 specimens were used to conduct monotonic, isothermal tests in strain control at a constant (shear) actual strain rate of $1x10^{-3}s^{-1}$ and at a constant temperature of 25°C, for an extremely short duration of 2 seconds, to minimize the influence of time-dependent (viscoplastic or anelastic) deformations on the results. Ten such tests were repeated on each specimen without uninstalling it to account for errors in measurement due to slippage of the specimen. The specimen was then flipped over and the measurements were repeated. This accounted for errors introduced in measurement due to misalignment of the machine grips. A force vs. strain curve was plotted for each specimen for each run. Figure 4.10 shows one such run for one specimen.

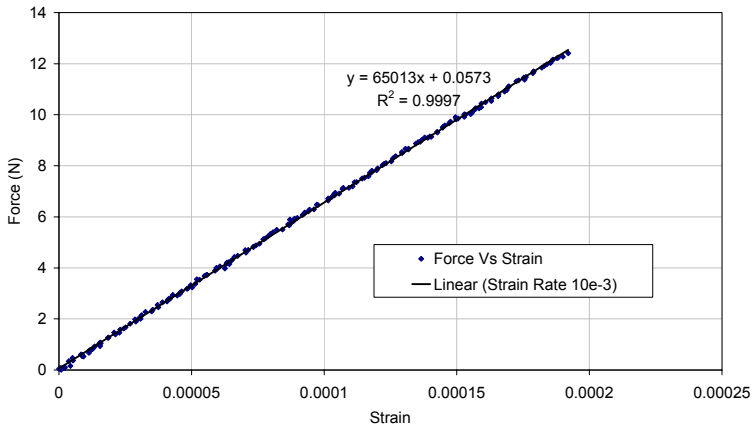

Fig. 4.10

Sample force vs. Strain curve for specimen A1-10 at 25°C for Method 1

The above plot clearly shows that the maximum value of the stress that the specimen experienced during the test was well below the yield stress of the material, for the corresponding strain rate, thus proving the validity of using such a test to measure modulus. The slope of the curves obtained for all the specimens was averaged, since there was a certain degree of scatter in the values from specimen to specimen. The compliance effects of the copper specimen were accounted for in the manner explained in section 2.5. The shear modulus was obtained from the ensuing force vs. strain curve and the elastic modulus, E, was then obtained from the relationship,

$$G = \frac{E}{2(1+\nu)} \tag{4.1}$$

where G is shear modulus calculated from the slope of the force vs. strain plot curve, and ν is the Poisson's ratio (ν = 0.4 for pure lead).

For example, the calculation of elastic modulus at 25^{o}C using method 1:

From force vs. strain curve for all specimens, averaged slope (S) = 52616N/ε.

Actual solder joint height (h) = 105.33μm.

Actual joint width (w) = 2.01mm.

Actual joint thickness (t) = 1.092mm.

Applied force (F_{app}) = 26N.

Extensometer gauge length (l) = 3mm.

From Figure 3.32, compensation rate ($CR\ [Cu]$) = 4.69x10^{-8}m/N, for t = 1.092mm.

From Equation (2.5), actual deformation of copper (δ_{AB}) = 1.22x10^{-6}m.

Measured strain by extensometer ($\varepsilon_{BB'}$), at 26N = F_{app}/S = 0.000494ε.

Measured deformation by extensometer ($\delta_{BB'}$) = $\varepsilon_{BB'} \times l$ = 1.48x10^{-6}m.

From Equation (2.6), actual deformation of solder ($\delta_{AA'}$) = 2.63x10^{-7}m.

Thus, shear stress (τ) = F/wt = 1.184x10^{7}N/m^{2}.

And shear strain (γ) = $\delta_{AA'}/h$ = 0.002497.

Shear Modulus (G) = τ/γ = 4.744x10^{9}N/m^{2} (Pa).

From Equation (4.1), Elastic Modulus (E) = 1.328x10^{10}N/m^{2} (Pa), i.e. 13.28GPa.

Method II

In the second method, 13 specimens were used to conduct monotonic, isothermal tests at 80^{o}C, 125^{o}C, and 150^{o}C at a constant shear strain rate of 1x10^{-3}s^{-1}, to obtain shear stress vs. strain curves as shown in Figures 4.2 through 4.5. The slope between the origin and a point within the elastic regime of the stress vs. strain curve was used to calculate the shear modulus, from which the elastic modulus was derived using Equation (4.1), in a manner identical to method 1. A comparison between the two methods showed a 5% difference in the slope, S. For example, Method I yielded an average slope of 55345 at 25^{o}C and a strain rate of 1x10^{-3}s^{-1}, and Method II an average slope of 52456, for the same temperature and strain rate. This resulted in an average Young's Modulus of 13.49GPa from Method I and an average Young's Modulus of 13.06GPa from Method II, a difference of less than 5%. Method II was used since it was possible to use the same data obtained from the constant strain rate tests conducted for estimation of the time-independent plastic and time-dependent creep properties for the estimation of Young's Modulus of Elasticity, thereby

reducing the overall number of tests conducted. Table 4.3 shows the values of Young's modulii obtained through combined methods 1 and 2 for the whole range of selected temperatures.

Temperature (T) ^{o}C	**Young's Modulus (G) GPa**		
	Maximum	***Average***	***Minimum***
25	14.61	13.28	12.10
80	10.46	9.27	8.35
125	8.40	7.34	6.42
150	7.19	5.81	4.27

Table 4.3: Elastic Modulus as a function of Temperature

Assuming a Poisson's Ratio of 0.4 [Source: www.matweb.com], a modulus of 13.28GPa was found for the 95.5Pb2Sn2.5Ag solder at room temperature, which is just lower than the modulus of pure lead (13.8GPa) [Source: www.matweb.com]. Figure 4.11 shows the dependence of elastic modulus on temperature. The elastic modulus showed a linear relationship with temperature. As expected, the value of Young's modulus decreased with increase in temperature due to the increased contribution of thermally activated processes such as creep deformation in reduction of strength of the solder joint.

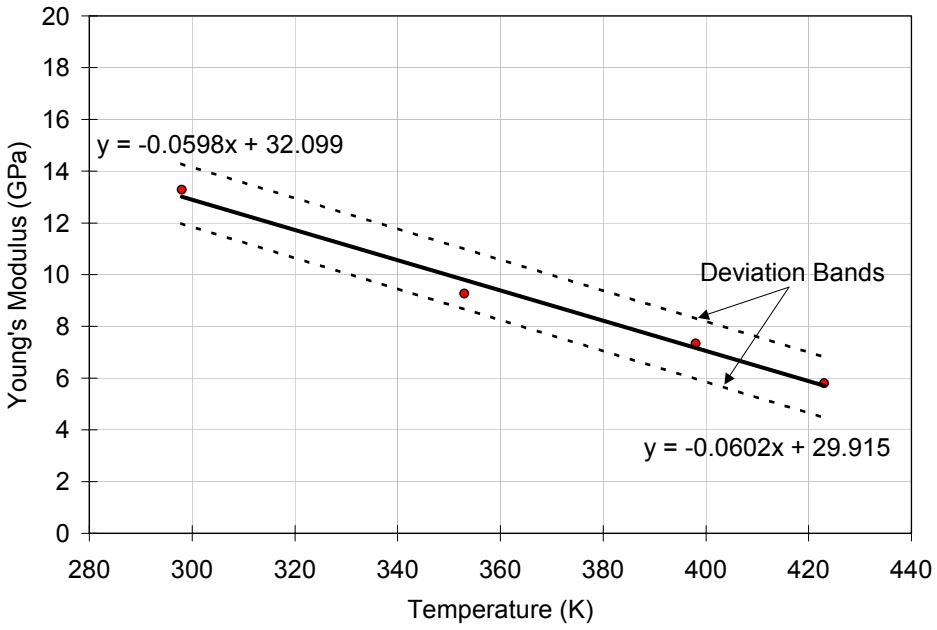

Fig. 4.11

Temperature dependence of elastic modulus, E

A modulus-temperature relationship for 95.5Pb2Sn2.5Ag solder alloy was obtained for the average value of modulii:

$$E = 30.448 - 0.0585T(K) \tag{4.2}$$

The range of the modulus-temperature relationship was also obtained. The equations (4.3) below show the modulus-temperature relationships for the obtained maximum and minimum values of Young's modulus:

$$\begin{aligned} E &= 32.099 - 0.0598T(K) \\ E &= 29.915 - 0.0602T(K) \end{aligned} \tag{4.3}$$

While these expressions represented the test data fairly well, the combined effects of the miniature specimen configuration, loading calibration effects, and the effects of inelastic and thermally activated deformations on the apparent solder deformation may well have had an effect on data interpretation. Thus, these results are recommended for use only in durability modeling. The values of the elastic constants obtained for Equation (2.10) are tabulated below:

Parameter	Maximum	Value	Minimum
E_0	32.099	30.448	29.915
E_T	0.0602(T)	0.0585(T)	0.0598(T)

Table 4.4. Elastic constants

Figure 4.12 below shows the temperature dependence of Young's Modulii of some high lead solders, in comparison with that of the 95.5Pb2Sn2.5Ag solder.

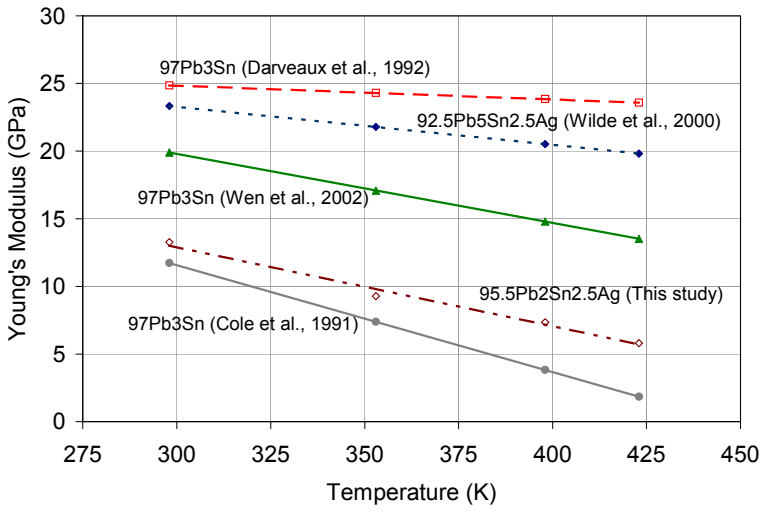

Fig. 4.12

Temperature dependence of Young's modulii of some lead-rich solders

It can be seen that the value of Young's modulii reported by different investigators differ even for alloys of the same composition. Several factors influence the measurement of Young's modulus including the loading rate, creep effects, specimen configuration, and the structural compliance of the load train. The Table below shows the values of Young's modulii for some lead-rich solders at room temperature as obtained by different investigators, as well as the assumed value of Poisson's ratio.

Solder	Specimen Type	Modulus at 25°C	Assumed Poisson's ratio	Source
92.5Pb5Sn2.5Ag	Cylindrical dog-bone	23.32GPa	0.33	Wilde et al., 2000
97Pb3Sn	Flip-chip assembly	24.84GPa	0.35	Darveaux et al., 1992
97Pb3Sn	Cylindrical dog-bone	11.73GPa	-	Cole et al., 1991
97Pb3Sn	Cylindrical dog-bone	19.89GPa	-	Wen et al., 2002

Table 4.5 Young's Modulii for lead-rich solders obtained from literature

4.4 Time-independent Plasticity

To determine plastic constants for 95.5Pb2Sn2.5Ag solder, results from isothermal, monotonic constant strain rate tests conducted on 54 specimens at actual shear strain rates of $1x10^{-2}s^{-1}$, $1x10^{-3}s^{-1}$, $1x10^{-4}s^{-1}$, $1x10^{-5}s^{-1}$, and $1x10^{-6}s^{-1}$, and temperatures of 25°C, 80°C, 125°C, and 150°C were used. Figure 4.13 is a plot of axial force vs. strain for a constant strain rate test at $1x10^{-4}s^{-1}$ and temperature of 25°C. These were converted into shear stress vs. shear strain curves using the following relations,

$$\tau = \frac{F}{wt} \text{ and } \gamma = \frac{\delta}{h}; \delta = \varepsilon l \tag{4.4}$$

where τ is the shear stress, F is the axial force, w is the joint width, t is the joint thickness, γ is the shear strain, δ is the deformation of the solder joint, h is the joint height, ε is the axial strain, and l is the gauge length of the extensometer. The compliance effects of the copper specimen were accounted for in the manner explained in section 4.2.

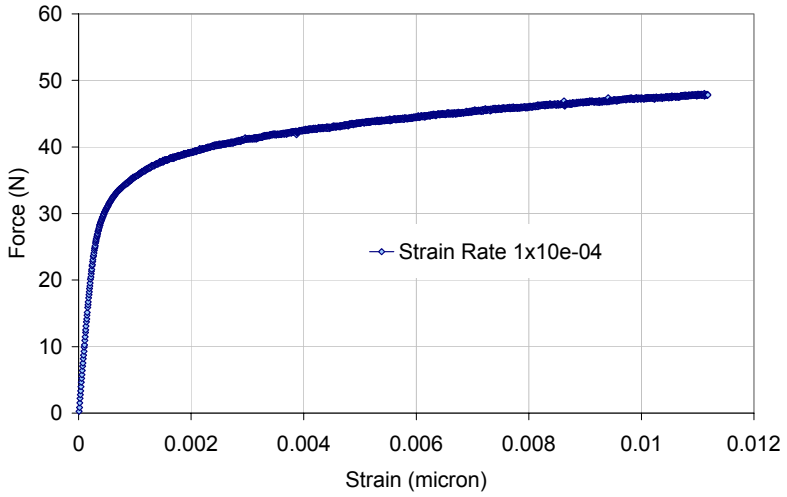

Fig. 4.13

Sample force vs. strain curve at a constant strain rate of $1x10^{-4}$ and temperature of $25^{o}C$

As seen from figures 4.2 through 4.5, the flow stresses at corresponding strains were strong functions of strain rate, with the stresses increasing with the strain rate due to less time being allowed for thermally activated processes. Since thermally activated processes occur faster at higher temperatures, the stresses at corresponding strains were progressively lower at $150^{o}C$ as compared to $25^{o}C$. Shear stress was converted

to equivalent tensile stress and shear strain was converted to equivalent tensile strain by applying the Von Mises yield criterion to obtain the relationships (repeated here for continuity),

$$\sigma = \tau\sqrt{3}, \varepsilon = \frac{1}{\sqrt{3}}\gamma \tag{2.15}$$

Using the methodology explained in Section 2.7 for calculating the strain rate independent stress, six values of strain were chosen for which the corresponding flow stress would be extrapolated, namely 0.5%, 0.75%, 1%, 2.5%, 5%, and 7.5%. Stress vs. strain rate curves were plotted for these values of strain, for each temperature. Figure 4.14 shows such a plot for 125°C.

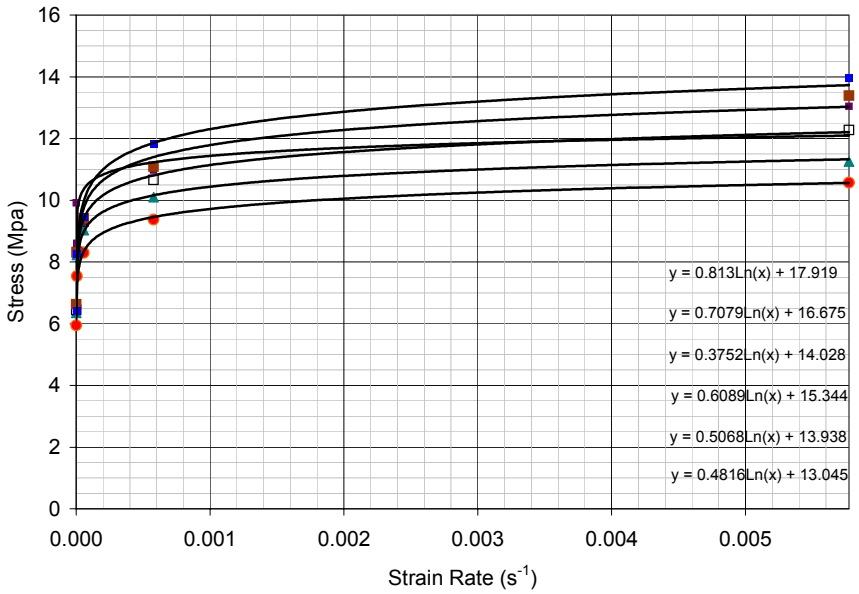

Fig. 4.14

Equivalent stress vs. strain rate plot for the chosen values of strain for converted strain rates of $1x10^{-2}s^{-1}$ through $1x10^{-6}s^{-1}$ and temperature of 125°C

A logarithmic curve was observed to provide the best fit to the test data. The values of equivalent stress obtained from the curve fit were extrapolated for very high strain rates. For this purpose the unrelaxed stress was defined as the value corresponding to the point where the slope of the extrapolated curve fell below 10^{-3}MPa-s. This rate-independent equivalent stress was then plotted against equivalent strain yielding a rate-independent stress vs. strain curve for each temperature. Figure 4.15 shows such rate-independent stress vs. strain plots for the whole selected range of temperatures.

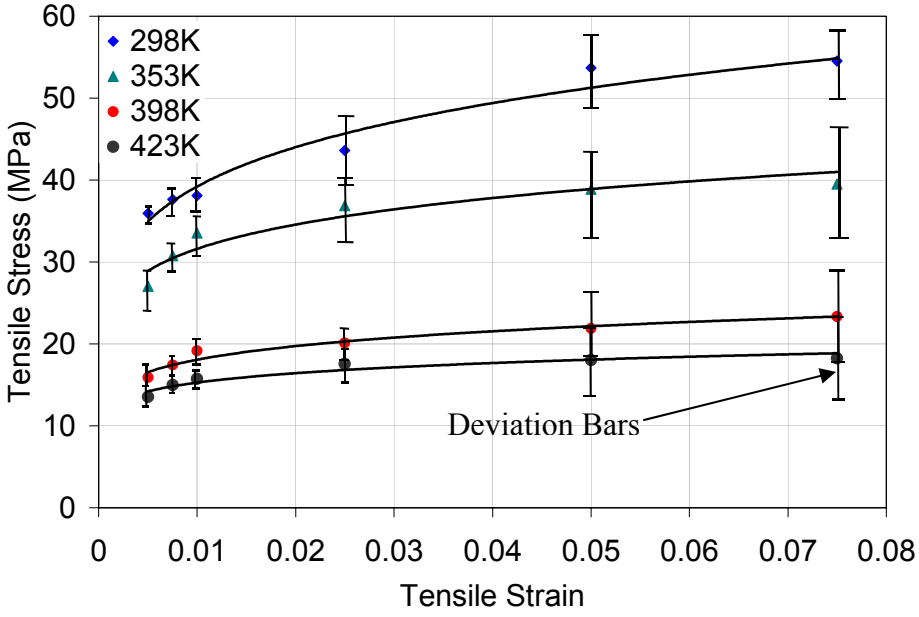

Fig. 4.15

Strain rate-independent equivalent tensile stress vs. equivalent tensile strain

A power law described in chapter 2 given by Equation (2.11) was fit to the above curves to obtain the constants n_p and K, which are the strain hardening exponent and the pre-exponential co-efficient respectively. The values of the plastic constants

obtained are tabulated below:

Temperature (T) ^{o}C	N_p			K		
	Max.	***Avg.***	***Min.***	***Max.***	***Avg.***	***Min.***
25^{o}C	0.2012	0.1665	0.1313	102.378	84.416	67.112
80^{o}C	0.1787	0.1291	0.0977	70.678	57.286	45.015
125^{o}C	0.1579	0.1268	0.0902	49.899	32.403	15.345
150^{o}C	0.1451	0.1048	0.0681	41.623	24.754	9.743

Table 4.6: Time independent plastic constants

The averaged values of the constants were obtained as a function of temperature for the 95.5Pb2Sn2.5Ag solder are shown below:

$$n_p = 0.2954 - 0.0004T(K)$$
$$K = 230.05 - 0.49T(K) \quad (4.5)$$

And the temperature dependencies obtained for the maximum and minimum values of the constants are expressed in equations (4.6) and (4.7) respectively:

$$n_p = 0.3223 - 0.0004T(K)$$
$$K = 246.09 - 0.4901T(K) \quad (4.6)$$

$$n_p = 0.2636 - 0.0005T(K)$$
$$K = 213.73 - 0.4884T(K) \quad (4.7)$$

Their respective temperature dependencies are plotted below in Figures 4.16 and 4.17.

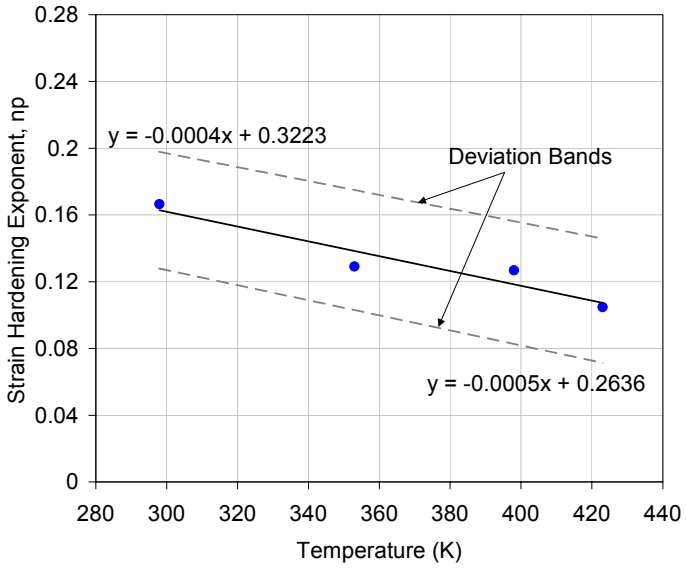

Fig. 4.16

Temperature dependence of strain hardening exponent

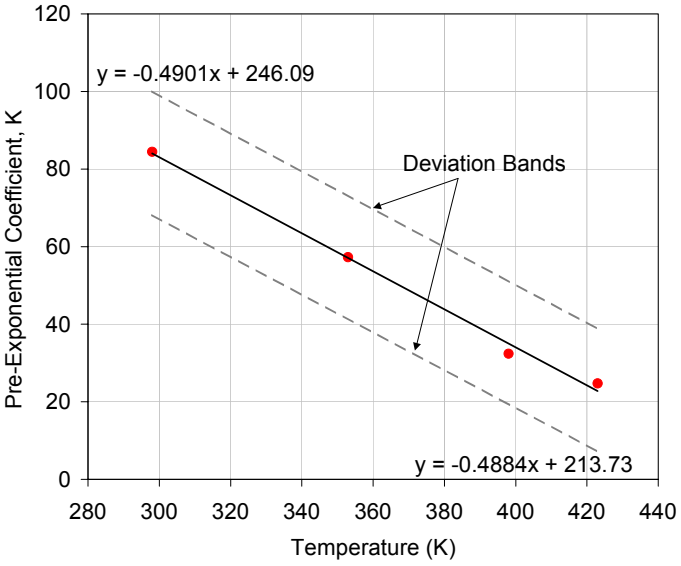

Fig. 4.17

Temperature dependence of pre-exponential co-efficient

A reasonable fit was obtained for the test data. Both the strain hardening exponent and the pre-exponential co-efficient decreased with increasing temperature, since at higher temperatures, thermally activated processes such as creep deformations could induce stress relaxation thereby reducing the strength of the joint. However, it should be noted that the contribution of time-independent plastic deformation to the total deformation of lead-rich solders is negligibly small. Therefore, even a small amount of variation in the acquired data may cause a relatively large change in the value of the time-independent plasticity constants.

4.5 Time-dependent Steady-state Creep

In a constant strain rate test, after the strain or loading time is sufficient, the strain hardening is nearly zero when the plastic flow reaches a steady state. Furthermore, the stress and deformation resistance are approximately the saturation values [Wilde et al., 2000]. This is analogous to the steady state saturation strain rate for a constant load/stress test [Zhang et al., 2003]. Thus, even from these experiments one can calculate the steady state strain rate and saturation stress pairs. Saturation stress was observed to be temperature and strain rate dependent.

Data from 54 specimens subjected to monotonic, isothermal, constant strain rate tests for a wide range of temperatures of 25°C, 80°C, 125°C, and 150°C, and strain rates of $1x10^{-2}s^{-1}$, $1x10^{-3}s^{-1}$, $1x10^{-4}s^{-1}$, $1x10^{-5}s^{-1}$, and $1x10^{-6}s^{-1}$ was used to model the time dependent plastic behavior that is creep. The saturation stress value was calculated for each strain rate and temperature. The results are summarized in table 4.7 below:

dγ/dt	**τ (Mpa)**											
	T = 298K			**T = 298K**			**T = 298K**			**T = 298K**		
	Max	***Avg***	***Min***	***Max***	***Avg***	***Min***	***Max***	***Avg***	***Min***	***Max***	***Avg***	***Min***
$1.00x10^{-2}$	20.5	19.1	18.0	15.7	14.8	13.9	10.1	9.60	9.03	8.42	7.70	6.96
$1.00x10^{-3}$	17.3	16.4	15.3	12.8	11.9	11.1	7.77	7.31	6.89	6.76	6.31	5.82
$1.00x10^{-4}$	14.6	13.8	13.1	9.98	9.36	8.85	6.83	6.29	5.93	5.64	5.21	4.86
$1.00x10^{-5}$	11.5	10.6	9.78	8.51	7.84	7.18	5.21	4.90	4.58	4.31	3.96	3.56
$1.00x10^{-6}$	9.78	9.07	8.34	7.10	6.50	5.93	4.35	3.99	3.67	3.60	3.19	2.80

Table 4.7: Saturation stress and strain rate pairs for different temperatures

These results were then converted to the equivalent tensile creep strain rate and corresponding equivalent tensile stress using equation (2.15) derived from Von Mises' yield criteria, and then plotted on a natural log-log scale as shown in Figure 4.18.

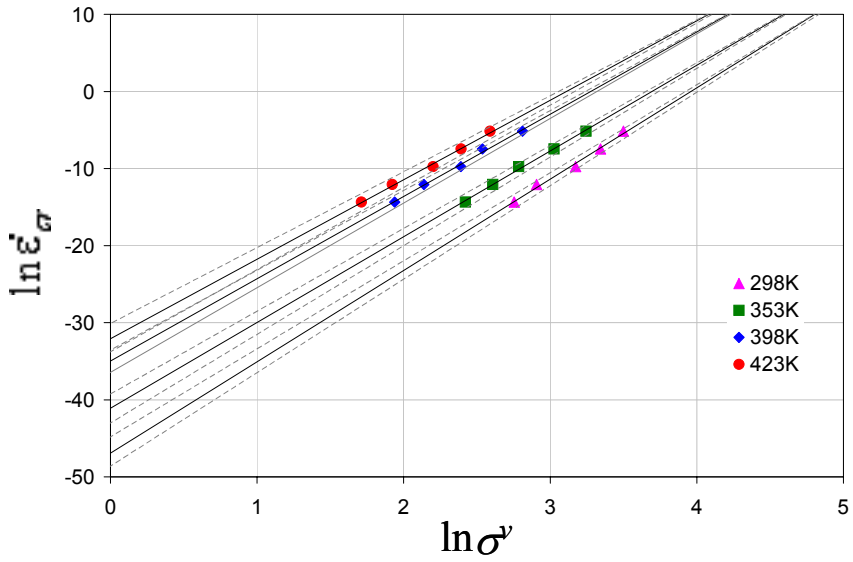

Fig. 4.18

Log-log plot of equivalent steady state creep strain rate and equivalent average saturated stress pairs

The slope of the strain rate vs. average saturated stress curves for different temperatures yielded the creep exponent and the intercept yielded the stress co-efficient and the thermal activation energy for creep, and was calculated as follows (repeated here for continuity),

$$\ln \dot{\varepsilon}_{cr} = \ln A - \frac{Q}{RT} + \frac{1}{n_c} \ln \sigma_v \qquad (2.16)$$

The parameters thus calculated for the whole range of temperatures are summarized in the table below:

Temperature (T)	$\frac{1}{n_c}$			$\ln A - \frac{Q}{RT}$		
	Max	***Avg***	***Min***	***Max***	***Avg***	***Min***
25°C (298K)	12.312	11.848	11.421	-49.932	-46.910	-43.899
80°C (353K)	11.490	11.123	10.673	-44.657	-41.094	-38.454
125°C (398K)	11.189	10.671	10.113	-37.823	-34.975	-32.720
150°C (423K)	10.823	10.308	9.814	-35.374	-32.061	-29.278

Table 4.8: Creep model parameters calculated from log-log plot

These parameters were then used to obtain their corresponding temperature dependency relationships from the plots shown in Figures 4.19 and 4.20. The obtained relationships are given by the equations,

$$\frac{1}{n_c} = 15.425 - 0.0121T(K)$$
$$(\ln A - \frac{Q}{RT}) = 2.4661 - 14903T(K) \quad (4.8)$$

The temperature dependencies of the maximum and minimum values of the parameters were also obtained as shown below in equations (4.9) and (4.10) respectively:

$$\frac{1}{n_c} = 15.67 - 0.0116T(K)$$
$$(\ln A - \frac{Q}{RT}) = 3.2162 - 13996T(K) \quad (4.9)$$

$$\frac{1}{n_c} = 15.211 - 0.0128T(K)$$

$$(\ln A - \frac{Q}{RT}) = 1.2514 - 15454T(K) \tag{4.10}$$

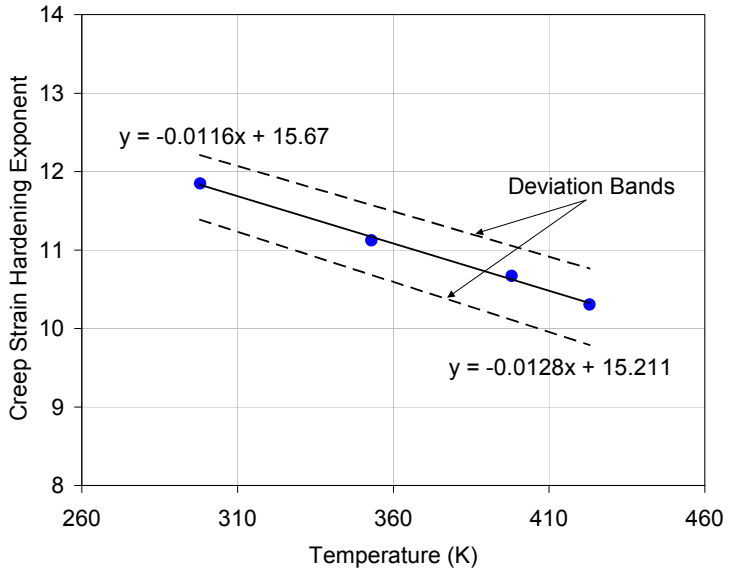

Fig. 4.19

Temperature dependence of creep exponent

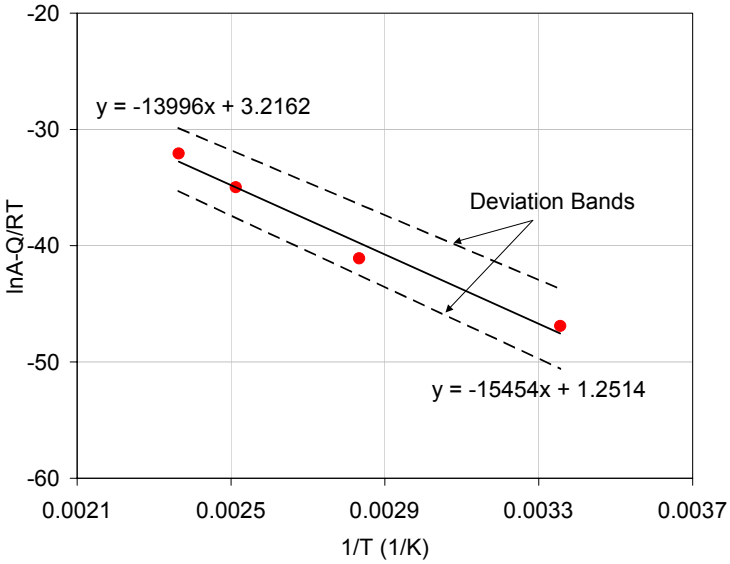

Fig. 4.20

Arrhenius plot to determine creep thermal activation energy

The stress co-efficient, A, was calculated from the y-intercept of the average curve in Figure 4.20, and the thermal activation energy, Q, was calculated from the slope of the same curve. The values are shown in Table 4.9 below:

Parameter	**Values**		
	Max	***Avg***	***Min***
A	24.933	11.776	3.495
Q	1.33eV	1.28eV	1.21eV

Table 4.9: Time dependent creep constants

The average value of the creep stress exponent that was obtained suggested dislocation climb controlled deformation. The average value of activation energy that was obtained is very close to that of lattice diffusion in pure lead (1.1eV). This is somewhat inconsistent with the obtained stress exponent. The probable reasons for this behavior are discussed in detail in section 4.6 below.

4.6 Discussion

Under shear loading, most solder alloys show a decrease in ductility as temperature is increased or strain rate is decreased [Darveaux et al., 1992]. This observation is consistent with a strain energy partitioning approach to cyclic fatigue damage, where the intent is to separately quantify damage due to elastic potential energy, plastic work and creep work. Typically, creep is considered significantly more damaging. Thus this section is devoted to understanding the mechanisms of creep deformation.

A creep deformation mechanism map for steady-state (secondary) creep is shown in Figure 4.21 [Frost et al., 1982], where the stress is normalized by the shear modulus.

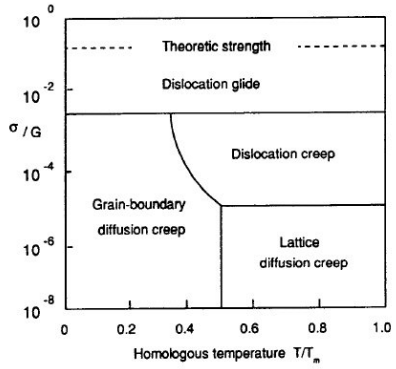

Fig. 4.21
Simplified creep deformation mechanism map

Lattice diffusion creep represents a creep mechanism controlled by atomic diffusion under application of very low stress and is usually called Nabarro-Herring creep [Dieter, 1986]. Usually, a stress not high enough to move dislocations but enough to trigger atoms or vacancies to migrate in preferential directions if $T > 0.5T_m$ (high homologous temperatures) causes lattice diffusion. At relatively higher stress and low homologous temperature ($T<0.5T_m$), lattice diffusion becomes progressively difficult. In this case, atoms or vacancies move easily in porous grain boundaries, since they less closely packed along the grain boundaries. This is known as *grain boundary diffusion* or *core diffusion*. At high stress levels and high homologous temperatures, creep rate is controlled by dislocation motion, causing deformation known as *dislocation creep* or *dislocation climb*. Dislocations in crystalline materials are activated to glide at the highest stresses. If other dislocations, precipitates or phase particles obstruct motion of the dislocations, then dislocation climb helps the

dislocations to continue gliding. In this case, gliding produces all the creep strain, while climbing controls the creep rate, since atomic diffusion controls climbing and the gliding rate is much faster than the diffusion rate. At intermediate values of stress and higher homologous temperatures, *grain boundary (GB) sliding* or *superplasticity* is known to occur. Here grains shear with respect to each other at the grain boundaries. The characteristic behavior of steady-state creep deformation kinetics of solder alloys at high homologous temperatures is shown schematically in Figure 4.22.

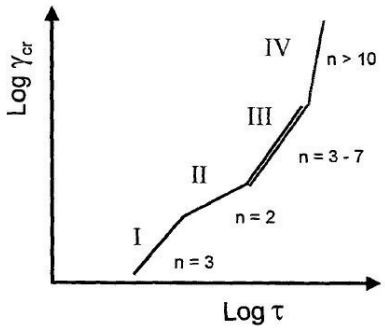

Fig. 4.22

Schematic of log-log plot of shear creep rate vs. applied shear stress (for steady state creep deformation of metals and alloys at high homologous temperatures [Hacke et al., 1997])

Regions I and II are grain (phase) size dependent whereas regions III and IV are not. Generally, investigators have focused their research on regions II and III, deformation within which is dominated by grain boundary sliding (superplasticity) and dislocation climb (matrix creep) respectively. Grivas et al. suggested that Pb-Sn eutectic alloys exhibit both superplasticity and matrix creep, simultaneously occurring through independent mechanisms. Superplasticity is rate controlling at lower stresses whereas matrix creep is rate controlling at higher values of stress [Schubert et al., 2001]. Stress exponents and activation energies found by various investigators using various

test specimens and methodologies for Pb-based solder materials are shown in Table 4.10 for comparison.

Solder alloy	Specimen Type	Model	Stress Exponent	Activation Energy (eV)	Creep Mechanism	Investigator
92.5Pb5Sn2.5Ag	Cylindrical dog-bone	Anand Model	-	0.95	Lattice diffusion	Wilde et al., 2000
92.5Pb5Sn2.5Ag	BGA solder joint	Creep power-law (low temp/ high temp)	11.59/8.34	-	Dislocation climb	Solomon, 1990
98Pb2Sn	Rectangular tensile	Weertman (high temp)	8.0	0.99	Lattice diffusion	Frost et al., 1988
98Pb2Sn	Rectangular tensile	Weertman (low temp)	13.0	0.46	Dislocation climb	Frost et al., 1988
97Pb3Sn	Flip-chip assembly	Modified hyperbolic sine	7.0	1.20	Dislocation climb	Darveaux et al., 1992
96.5Pb3.5Sn	Cylindrical dog-bone	Weertman	13.0	0.75	Dislocation climb	Wen et al., 2002
96.5Pb3.5Sn	Rectangular tensile	Weertman (high temp)	5.0	0.99	Lattice diffusion	Frost et al., 1988
96.5Pb3.5Sn	Rectangular tensile	Weertman (low temp)	6.5	0.62	Dislocation climb	Frost et al., 1988
95Pb5Sn	Flip-chip assembly	Modified hyperbolic sine	7.0	1.20	Dislocation climb	Darveaux et al., 1992
95Pb5Sn	Rectangular tensile	Weertman (high temp)	7.0	0.67	Lattice diffusion	Frost et al., 1988
95Pb5Sn	Rectangular tensile	Weertman (low temp)	7.0	0.62	Dislocation climb	Frost et al., 1988
90Pb10Sn	Rectangular tensile	Weertman (high temp)	5	0.67	Lattice diffusion	Frost et al., 1988
90Pb10Sn	Rectangular tensile	Weertman (low temp)	3.0	0.62	Dislocation climb	Frost et al., 1988
63Sn37Pb	Actual solder assemblies	Partitioned creep	2.0/7.1	0.5/0.84	GB sliding/ matrix creep	Grivas et al., 1979
63Sn37Pb	Actual solder assemblies	Partitioned creep	1.7/11.1	0.46/1.0	GB sliding/ matrix creep	Kashyap et al., 1981
63Sn37Pb	-	Partitioned creep	3.1/7.3	-	GB sliding/ matrix creep	Solomon, 1986
63Sn37Pb	Actual solder assemblies	Partitioned creep	2.4/5.7	0.45/0.9	GB sliding/ matrix creep	Lam et al., 1979
63Sn37Pb	-	Partitioned creep	3.0/7.0	0.47/0.47	GB sliding/ matrix creep	Wong et al., 1988
63Sn37Pb	Cylindrical dog-bone	Modified hyperbolic sine	5.0/3.0	0.5/0.84	Dislocation glide/ lattice diffusion	Shi et al., 2001
63Sn37Pb	Cylindrical dog-bone	Weertman-Dorn	2.0/7.1	0.5/0.84	GB sliding/ matrix creep	Hacke et al., 2001
62Sn36Pb2Ag	Flip-chip assembly	Modified hyperbolic sine	3.3	0.55	Dislocation viscous glide	Darveaux et al., 1992
60Sn40Pb	Flip-chip assembly	Modified hyperbolic sine	3.3	0.55	Dislocation viscous glide	Darveaux et al., 1992
59Sn40Pb1Ag	Cylindrical dog-bone	Weertman-Dorn	1.87/6.74	0.5/0.79	GB sliding/ matrix creep	Schubert et al., 2001

Table 4.10: Comparison of creep model parameters obtained from literature

As observed in the table on the previous page, there is a marked difference in values of activation energy and stress exponent as observed by different investigators. There are several factors contributing to the large variation in measured parameters, including type of specimen, geometry and loading constraints of specimen/solder joint, the specimen preparation procedure and conditioning (aging), resulting microstructure and grain size of the alloy, intermetallic compound formation, type of test and manner in which it was conducted, temperatures and strain rates used, measurement calibration and accuracy (gauge length), modeling methodology used to fit experimental data, and underlying assumptions of mechanical properties of material, such as shear modulus and Poisson's ratio. Furthermore, the stress exponent is larger in the high stress regime than it is in the lower stress regime at any given temperature. This phenomenon is known as *power-law breakdown*. The activation energy if determined from different points on one single curve can be different for the same stress level [Shi et al., 2001].

Often, more than one creep mechanism operates simultaneously. If several mechanisms are mutually dependent, the fastest mechanism governs the creep behavior, while if the mechanisms act independently, then the slowest mechanism governs the creep behavior [Li et al., 1993]. Thus, even though the deformation mechanism responsible for the creep deformation may be dislocation climb as indicated by the high stress exponent, the deformation rate is governed by the atomic lattice diffusion. Further testing conducted at lower shear strain rates of $1x10^{-7}s^{-1}$ to

$1x10^{-9}s^{-1}$ and temperatures upto 200°C may provide some clarifications. As a representative result, Figure 4.23 shows the comparison of experimental data and the prediction from the Weertman Model.

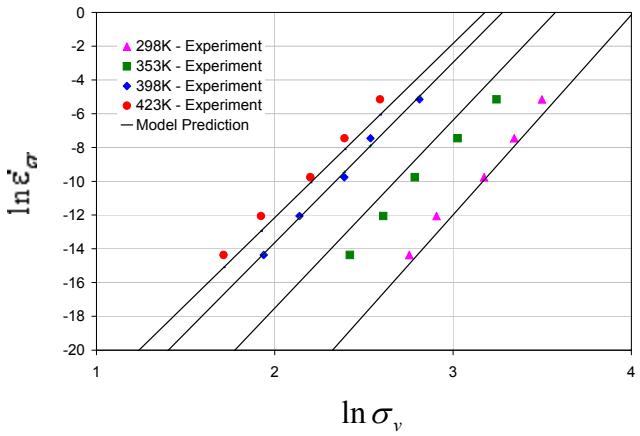

Fig. 4.23

Comparison of model prediction and experimental data for steady-state creep behavior

A good agreement between the experimental data and the model predictions was achieved for the assumed test conditions. Some deviations from the experimental data and model predictions were observed as expected: the model consistently underestimated the stresses at 80°C, and slightly overestimated the stresses at 150°C compared with experimental data. Nevertheless, the model represented the creep deformation behavior quite well.

Conclusions

Components of a power electronic device, including the die attach experience operating temperatures as high as 200^{o}C, which may cause significant reliability concerns. The common eutectic Sn-Pb solder cannot fulfill these service requirements, and one must turn to solder alloys with higher melting points such as the Pb-rich alloys, which have a melting point in the range of 300^{o}C. Before the reliability of any system can be accurately predicted for the field conditions, one has to be able to accurately predict the reliability of critical components of the system, once they have been identified. The die attachment material of a power electronic device is one of the weak links in the system. Durability characterization is essential in order to accurately predict the reliability of the solder alloy chosen for the die attach material under life cycle loads. However, relevant constitutive property measurements must be carried out, as these are essential for quantitative characterization of damage accumulation, the knowledge of which is essential for accurate durability assessment.

The solder chosen for constitutive measurements is one of the commonly used high temperature solders, namely the 95.5Pb2Sn2.5Ag solder alloy. Constitutive property measurements of 95.5Pb2Sn2.5Ag solder have been conducted by adapting an existing specimen configuration and test methodology developed for constitutive property measurements of lead-free solder alloys used as controlled collapse chip connection (C4) in small signal electronic devices.

A specimen with a solder joint of nominal dimensions 2mm x 1.5mm x 100μm designed to simulate geometrical and loading constraints in a die attach was utilized for testing on a uniaxial MTS Tytron^{TM} 250 Microforce testing machine. The specimen preparation procedure was improved to obtain optimum solder joint quality before commencement of testing to enhance repeatability of test data.

Monotonic, isothermal tests were conducted at constant shear strain rates of $1x10^{-2}s^{-1}$, $1x10^{-3}s^{-1}$, $1x10^{-4}s^{-1}$, $1x10^{-5}s^{-1}$, and $1x10^{-6}s^{-1}$, and at temperatures of 25^{o}C, 80^{o}C, 125^{o}C, and 150^{o}C to obtain the temperature and strain rate dependent mechanical properties such as Yield stress and Ultimate tensile strength, as well as the time-independent elastic and plastic, and the time-dependent creep constitutive properties of the solder alloy.

A partitioned constitutive approach was chosen for modeling purposes. The material specific parameters of the models were extrapolated from the experimental data by suitably curve fitting the data, and reasonable fits were obtained. Special attention was given to creep deformation, since for solder alloys creep deformations contribute most of the damage accumulated during cyclic fatigue at high homologous temperatures. Diffusion mechanisms for creep deformation were discussed and the diffusion mechanism(s) responsible for creep deformation in 95.5Pb2Sn2.5Ag solder, for the given test conditions, was (were) identified. The creep model predictions were then compared with the experimental data, and a good agreement was achieved.

Contributions

1. First program to employ the MTS Tytron^{TM} 250 Tester for measuring mechanical properties of ternary 95.5Pb2Sn2.5Ag solder alloy used as die attach in high temperature and high power applications.
2. First implementation of a direct local strain measurement technique (DLMT) developed by Kwon et al. [2003] for constitutive property measurement of lead-free solder alloys using the MTS Tytron^{TM} 250 Tester, for measuring the constitutive properties of 95.5Pb2Sn2.5Ag solder.
    a. Customized a miniature modified Iosipescu single-lap micro-shear specimen designed for simulating geometrical and loading constraints of a C4 joint in SMT, to simulate the constraints present in a large area die attach used in power packaging, by suitably altering the solder joint geometry.
    b. Modified the specimen preparation procedure to account for differences arising due to joint height and phase transition temperature.
    c. Obtained temperature and strain rate-dependent mechanical properties for 95.5Pb2.Sn.25Ag solder alloy such as Yield stress and Ultimate tensile strength.
    d. Determined the partitioned time-independent elastic, time-independent-plastic, and the time-dependent creep properties for a range of temperatures and strain rates.

Appendix A - Testing Procedures Using MTS Tytron™ 250

A.1 Machine Pre-start Instructions

To start operating the machine, the station manager must first be invoked.

- Select the *MTS Teststar*® icon on the PC desktop.
- Open the *Station Manager* – A dialog window titled *open station* appears.
- Use any existing configuration and choose a parameter set, or create a new configuration and define new user specific parameter set (consult *Model 793.10 MutiPurpose TestWare* manual).

Safety goes hand in hand with the operation of any machine and the Tytron is no exception. It is highly recommended that one follow this pre-start checklist before switching on the machine and operating it.

- *Read the available Manuals-*
    - Tytron 250 Microforce Test System (Hardware)
    - Model 793.10 MutiPurpose TestWare
    - Controller Installation and Calibration
    - Model 793.00 Software Installation
    - Axial Extensometer Product Information
    - System Software
- *Check all cable connections-*

  Consult the installation manual, and check if all the cable connections between the machine, the digital controller, the amplifier, and the PC,

including the ethernet cable connection, are correctly in place.

- *Load or re-load the TestStar IIs digital software-*

  If the service light is on, the TestStar IIs system software must be re-loaded before the machine can be operated.

- *Locate and connect the Emergency Interlock device (Remote Station Control)-*

  This device allows the operator to switch off the machine in case of any emergency, with the push of a single button.

- *Choose the correct force transducer to install-*

  Install the 250N or 10N load cell and corresponding cable depending on application.

- *Check Air supply-*

  Before switching on the machine, make sure that the air supply is on, and the air pressure is 100psi.

- *Install actuator runaway protector-*

  This is a small fixture, which fits into the T-slot on the test bed. It protects the force transducer by stopping the actuator in the case of runaway.

- *Install temperature chamber-*

  Install if required, along with the heating ducts and water pipes for keeping the remaining components of the machine cool. Turn on water supply. Use long grips for high temperature configuration.

- *Ensure that machine is switched on only in displacement control-*

  This is extremely important since the machine is started without loading the specimen and there is no protection against impact with the force transducer in

case of actuator runaway. Displacement control ensures that the actuator motion is restricted.

- *Set all appropriate interlocks*-

  Check for the maximum and minimum values for displacement, force and strain, and set appropriate interlocks.

- *Keep hands clear of the path of the actuator at al times*-

  The actuator speeds can be very high and body parts that come in the way of the actuator can be crushed against the reaction fixture.

A.2 Tuning

The machine requires *tuning* values for each control mode viz. displacement, force, strain and temperature for each new specimen material and geometry before commencement of actual testing. These tuning values are a distinct set of PID (proportional-integral-derivative gains) values for the chosen cyclic frequency of oscillation. These PID values can be manipulated using given controls and the response of the machine is measured through the oscilloscope. The aim is to make the mean, amplitude, peak, and valley of the measurable output value be as close to the desired output value of displacement, force, or strain, at the same time keeping the error down to a minimum, for a particular input value of displacement, force, or strain. Tuning values for the 95.5Pb2Sn2.5Ag solder are shown in Table A.1.

Tuning Mode	Device	P	I	D
Displacement ±60mm range (w/o specimen)	LVDT	1.75	1.85	0.042
Force ±250N	Transducer	1.00	2000.00	0.001
Displacement ±5mm range	LVDT	1.20	3400.00	0.001
Strain 8% range	Extensometer	2.00	50000.00	0.001

Table A.1: Tuning Values for 95.5Pb2Sn2.5Ag solder micro-shear lap specimen

A.2.1 Displacement Mode Tuning Without Specimen

The machine must first be tuned without the installation of any specimen, with just the grips or clamps in place. This ensures that the machine is in stable operating condition when the actuator is first switched on. The following steps should be followed for displacement tuning without installation of specimen:

- Set Target Set-point=0.00mm; Amplitude=2mm; Frequency=1Hz in the Function Generator of the Station Manager.
- Set privilege level to *Tuning* from the drop down list on the Station Manager window (password- *Tuning*; case-sensitive).
- In the *Station Set-up* window, go to //station/channels/axial/displacement/. In *Channel input signals* set the Current Range to ±60mm for Displacement.
- Set the *limits* as ±20mm and set the *Manual Offset* in *Offset-zero* to zero.
- Select the manufacturer specified initial tuning values of P=1.0, I=0.1 & D=0.001 in *Channel Tuning*.
- Set the *Meters* to give *Timed, Mean/Amplitude, and Peak/Valley* values for Displacement. Select appropriate units.

- Switch the machine on by clicking on the HSM1 button on the Station Manager. If the machine becomes unstable at any point of time (rapid vibrations/oscillations), press the red button on the *Remote station control* immediately.
- Click on the button for Manual Control in the Manual Command window to *enable* Manual Command.
- Set Manual Command *Displacement* to *Zero*.
- *Disable* Manual Command.
- Set *Signal Auto Offset* as zero for displacement, force and strain.
- Set the parameters for the *Scope*: Control Channel – Axial; Control Signal – Displacement; Response Signal – Axial; Response Signal – Error; and then *Re-scale*.
- Switch on the *Function Generator* by depressing the PLAY button.
- The actuator will oscillate with the specified Target Set-point, Amplitude, Frequency and Range, according to the selected PID gain values.
- The command displacement signal will be a *Triangular wave* in *red* and error signal should be a *Square wave* in *blue* if the selected waveform in Station Manager is *Ramp*.
- Now alter PID values slowly to match the output displacement for the timed, mean/amplitude and peak/valley values with the command input values, and to minimize the error value, to consequently obtain reasonably good waveforms. Make a note of PID values obtained.
- Never set PID values to zero; machine will become unstable.

- Never drag the cursor to change the PID values.
- Stop the function generator.

A.2.2 Force Mode Tuning With Specimen

- Continuing from the previous section, go the *Station Set-up* window to //station/channels/axial/force/ without switching off the machine. In *Channel input signals* set the Current Range to ±250N and set the *Manual Offset* in *Offset-zero* to zero.
- Set the *limits* as ±200N and set the *Manual Offset* in *Offset-zero* to zero.
- Set the values of P=1.0, I=0.50 & D=0.001 in *Channel Tuning*.
- Set Target Set-point=6N; Amplitude=4N; and Frequency=1Hz.
- Install the specimen between the grips. Do not clamp down.
- Enable *Manual Command*. Change the control mode to *Force* in the *Manual Command*.
- Tighten the clamps with the magnetic *clamp support* mounted in place so as to avoid breaking the specimen due to bending of the axis.
- Change the parameters in the Meters to give *Timed, Mean/Amplitude, and Peak/Valley* display for Force instead of displacement.
- Similarly, set the control signal to *Force* in *Scope* and *re-scale*.
- Set *Force* to zero in *Manual Command*.
- Set *Signal Auto Offset* as zero for displacement, force and strain.
- Start the Function generator.

- Now alter PID values slowly to match the output force for the timed, mean/amplitude and peak/valley values with the command input values, and to minimize the error value, to consequently obtain reasonably good waveforms. Make a note of PID values obtained.
- Stop the function generator.

A.2.3 Displacement Mode Tuning With Specimen

- Continuing from previous section, in the *Station Set-up* window, go to //station/channels/axial/displacement/. In *Channel input signals* set the Current Range to ±5mm for Displacement.
- Set the *limits* as ±2mm. *DO NOT* set the *Manual Offset* in *Offset-zero* to zero.
- Set the values of P=1.00, I=0.50 & D=0.001 for displacement in *Channel Tuning*.
- Change the control mode back to displacement in function generator.
- Set Target Set-point=0.01mm; Amplitude=0.01mm; Frequency=1Hz.
- *Enable* Manual Command.
- Change the control mode in Manual Command to displacement.
- *DO NOT SET* Manual Command Displacement to zero.
- *Disable* Manual Command.
- Set *Signal Auto Offset* as zero.
- Change the parameters in the Meters to give *Timed, Mean/Amplitude, and Peak/Valley* display for displacement instead of Force, using appropriate units.

- Similarly, set the control signal to *Displacement* in *Scope* and *re-scale*.
- Start the function generator.
- Now alter PID values slowly to match the output displacement for the timed, mean/amplitude and peak/valley values with the command input values, and to minimize the error value, to consequently obtain reasonably good waveforms. Make a note of PID values obtained.
- Stop the function generator.

A.2.4 Strain Mode Tuning With Specimen

- Ensure that the extensometer is securely attached to the specimen.
- Continuing from previous section, in the *Station Set-up* window, go to //station/channels/axial/strain/, without stopping the machine. In *Channel input signals* set the Current Range to ±8.0% for Strain.
- Set the *limits* as ±8.0%. *DO NOT* set the *Manual Offset* in *Offset-zero* to zero.
- Set the values of P=1.00, I=0.50 & D=0.0001 for strain in *Channel Tuning*.
- Change the control mode to strain in function generator.
- Set Target Set-point=100με; Amplitude=100με; Frequency=1Hz.
- *Enable* Manual Command.
- Change the control mode in Manual Command to strain. *DO NOT SET* Manual Command strain to zero.
- *Disable* Manual Command.
- Set *Signal Auto Offset* as zero.

- Change the parameters in the Meters to give *Timed, Mean/Amplitude, and Peak/Valley* display for strain, using appropriate units.
- Set the control signal to *Strain* in *Scope* and *re-scale*.
- Start the function generator.
- Now alter PID values slowly to match the output strain for the timed, mean/amplitude and peak/valley values with the command input values, and to minimize the error value, and consequently obtain reasonably good waveforms.
- Stop the function generator.
- Stop the machine.
- Return the control mode to Displacement in Manual Command and in Function generator.
- Save the PID values obtained for displacement, force, and strain modes for the new specimen in a logbook.
- Remember to follow pre-start instructions next time the machine is operated.

A.3 Measurement Calibration

The MTS TytronTM is a uni-axial testing machine. The force transducer measures axial force and the miniature extensometer measures axial strain. In order to apply a particular shear strain rate on the solder joint during any experimental run, the machine must be instructed to apply a corresponding actuator (crosshead) axial strain rate.

For example, to convert a shear strain rate of $1x10^{-5}s^{-1}$ to the corresponding axial strain rate, the following procedure is followed:

Desired actual shear strain rate ($d\gamma/dt$): $1x10^{-5}s^{-1}$

Solder Joint Height (h): 106.33μm

Gauge length (l): 3mm

Back-calculated actuator axial strain rate ($d\varepsilon/dt$):

$$d\varepsilon/dt = (d\gamma/dt)\frac{h}{l\times 1000} \tag{3.1}$$

$$= \left(1\times 10^{-5}\right)\frac{106.33}{3\times 1000}$$

$$= 3.54433\times 10^{-7}\,s^{-1}$$

Thus to apply an actual shear strain rate of $1\times 10^{-5}\,s^{-1}$ on the solder joint, the machine is instructed to apply an axial strain rate of $3.54433\times 10^{-7}\,s^{-1}$. Figure A.1 serves to validate that the back-calculated actuator axial strain rate applied by the machine is correct as calculated.

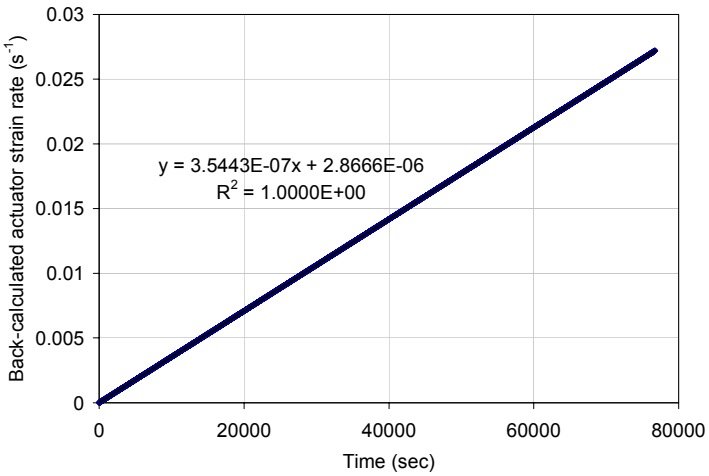

Fig. A.1

Applied actuator axial strain rate

A.4 Constant Strain Rate Test Procedure

During any test, instructions are conveyed to the machine through a stored procedure. Usually, the control mode, the absolute end-level of the applied load, the temperature, the data acquisition time, the various output parameters to be monitored, and the name and location of the output files is specified in these procedures. The data acquisition time is particularly important. For a higher shear strain rate of say, $1x10^{-1}s^{-1}$, the data acquisition time must be very short, to ensure that sufficient data points are gathered in order to obtain a smooth stress-strain curve. However, for a low shear strain rate of say, $1x10^{-6}s^{-1}$, one must exercise caution so as to not exceed the resolution of the extensometer (2.44με for 8.0% strain range). Table A.2 shows the data acquisition times used for the different shear strain rates.

Actual shear strain rate (s^{-1})	Data acquisition time (sec)	Minimum resolution required (με)	Extensometer resolution (με)
$1x10^{-2}$	0.01	3.75	2.44
$1x10^{-3}$	0.1	3.75	2.44
$1x10^{-4}$	1.0	3.75	2.44
$1x10^{-5}$	10.0	3.75	2.44
$1x10^{-6}$	100.0	3.75	2.44

Table A.2: Data Acquisition times for different strain rates

For example, a constant strain rate test conducted on a specimen with a solder joint height of 106.33μm, at an actual shear strain of $1x10^{-5}s^{-1}$ and 125°C, will have the following essential specifications:

Test Type: Ramp

Channel: Axial

Control Mode: Strain

Duration: 1000000sec

Absolute End level: $3.54433\times10^{-7}\,s^{-1}\times1000000 = 354433.33\,\mu\varepsilon$ (from section 3.3.3)

Channel: Temperature: 125°C

Data acquisition time: 10sec

Output values: Axial force, axial strain, time, and temperature

Once the procedure has been stored, the following steps will assist in conducting a typical constant strain rate test. Remember to follow all pre-start instructions.

- In the *Station Set-up* window, go to //station/channels/axial/displacement/. In *Channel input signals* set the Current Range to ±60mm for Displacement.
- Set the *limits* as ±20mm and set the *Manual Offset* in *Offset-zero* to zero.
- Select tuning values of P=1.75, I=1.85 & D=0.042 in *Channel Tuning*.
- In the *Station Set-up* window, go to //station/channels/axial/force/. In *Channel input signals* set the Current Range to ±250N for Force.
- Set the *limits* as ±200N and set the *Manual Offset* in *Offset-zero* to zero.
- Select tuning values of P=1.0, I=2000.0 & D=0.001 in *Channel Tuning*.
- In the *Station Set-up* window, go to //station/channels/axial/strain/. In *Channel input signals* set the Current Range to ±8.0% for Strain.
- Set the *limits* as ±8.0% and set the *Manual Offset* in *Offset-zero* to zero.
- Select tuning values of P=2.0, I=50000.0 & D=0.001 in *Channel Tuning*.
- Set the *Meters* to give *Timed, Mean/Amplitude, and Peak/Valley* values for Displacement, strain, and force. Select appropriate units.
- Switch on temperature controller and set desired temperature in manual command.
- Switch the machine on by clicking on the HSM1 button on the Station Manager. If the machine becomes unstable at any point of time (rapid vibrations/oscillations), press the red button on the *Remote station control* immediately.
- Click on the button for Manual Control in the Manual Command window to *enable* Manual Command.
- Set Manual Command *Displacement* to *Zero*.

- *Disable* Manual Command.
- Run the actuator at least 10 minutes to warm the machine up (e.g. In function generator, you can run cyclic test in displacement control below the maximum displacement range).
- Stop the function generator after machine has warmed up.
- Set displacement to zero in *Manual Command*.
- Install specimen, do not clamp.
- Change control mode to *force* in manual command.
- Clamp down specimen tightly, with assistance from magnetic clamp support.
- Remove support and set *Signal Auto Offset* as zero for displacement, force and strain.
- Close lid of temperature chamber and let temperature stabilize at desired level.
- In station manager, select MPT instead of Function generator, and select the desired procedure from the menu.
- Select a suitable name, preferably following a nomenclature, for the current run, and location for saving the output .dat files.
- Save parameters.
- Run test by pressing PLAY in the MPT TestWare.
- Monitor the displacement, force, and strain values through the meter.
- If desired, suitable force vs. time, or strain vs. time plots can be generated real-time through the MPT procedure (consult Model 793.10 MPT TestWare manuals for details).

REFERENCES

Alom, M. O., Chan, Y. C., Hung, K. C., *Reaction Kinetics of Pb-Sn and Sn-Ag solder balls with electroless Ni-P/Cu pad during reflow soldering in microelectronics packaging*, Proc. of 52nd ECTC, May 2002, pp. 1650-1657.

Anand, L., *Constitutive Equations for the Rate-dependent Deformation of Metals at Elevated Temperatures*, ASME Journal of Engineering Materials & Technology, Vol. 104, pp. 12-17, 1982.

Arrowood, R., Mukherjee, A., Jones, W., *Hot deformation of two-phase mixtures*, Solder Mechanics: A state of the art assessment, Frear, Jones, Kinsman (eds.), The Minerals, Metals, and Materials Society, 1991.

ASTM Standard D5379/D5379M-98 (1998), *Standard Test Method for Shear Properties of Composite Materials by the V-Notched Beam Method*, American Society for Testing and Materials, West Conshohocken, Pennsylvania (first published in May 1993).

ASTM Standard E1012-99, *Standard Practice for Verification of Specimen Alignment under Tensile Loading*.

Chan, Y. C., So, A. C. K., Li, J. K. L., *Effect of intermetallic compounds on the shear fatigue of Cu/63Sn-37Pb solder joints*, IEEE Trans. CPMT - Part B, 20, 1997, pp. 463-469.

Chan, Y. C., So, A. C. K., Li, J. K. L., *Growth kinetic studies of Cu-Sn intermetallic compound and its effect on the shear strength of LCCC SMT solder joints*, Materials Science and Engineering - Part B, 55, 1998, pp. 5-13.

Cole, M. S., Caulfield, T., Gonya, S. G., *Constant strain rate tensile properties of various lead based solder alloys at 0, 50, and 100^{o}C*, Proc, of 4th Electron. Mater. Process. Congr., Montreal, QC, Canada, 1991, pp. 241-249.

Cutiongco, E. C., Vaynman, S., Fine, M. E., Jeannotte, D. A., *Isothermal fatigue of 63Sn-37Pb solder*, ASME Journal of Electronic Packaging, Vol. 112, No. 2, 1990, pp. 110-114.

Darveaux, R., Banerji, K., *Constitutive Relations for Tin-based Solder Joints*, Proc. of the 42nd Electronic Components and Technology Conference, May 1992, pp. 538 – 551.

Darveaux, R., *Crack initiation and growth in surface mount solder joints*, Proc. of ISHM, 1993, pp. 86-97.

Darveaux, R., Banerji, K., Mawer, A., Dody, G., *Reliability of plastic ball grid array technology*, Ball grid array technology, Lau, J., H. (ed.), McGraw-Hill, New York, 1995, pp. 379-442.

Darveaux, R., *Solder joint fatigue life modeling*, Design and Reliability of solders and solder interconnections, The Minerals, Metals, and Materials Society, 1997, pp. 213-218.

Dasgupta, A., Oyan, C., Barker, D., Pecht, M., *Solder creep-fatigue analysis by an energy-partitioning approach*, ASME JEP, Vol. 114, No. 2, 1992, pp. 152-160.

Dieter, G., *Mechanical Metallurgy*, McGraw-Hill, New York, 3rd Ed., 1986.

Enke, N. F., Kilinski, T. J., Schroeder, S. A., Lesniak, J. R., *Mechanical behavior of 60/40 Tin-lead solder lap joints*, IEEE Trans. on CHMT, Vol. 12, No. 4, pp. 459-468.

Frear, D. H., *Microstructure and mechanical properties of solder alloys*, Solder Joint Reliability – Theory and applications, ed. Lau, Van Nostrand Reinhold, New York, 1991, pp. 266-278.

Frear, D. H., *The mechanical behavior of interconnect materials for electronic packaging*, Journal of Metals, Vol. 48, No. 5, 1996, pp. 46-53.

Frost, H. J., Ashby, M. F., *Deformation-mechanism maps*, Pergamon Press, 1982.

Frost, H. J., Howard, R. T., Lavery, P. R., Lutender, S. D., *Creep and tensile behavior of Lead-rich lead-tin solder alloys*, IEEE Trans. on CHMT, Vol. 11, No. 4, December 1988, pp. 371-379.

Fusaro, J. M., Darveaux, R., *Reliability of copper base-plate high current power modules*, Int. Journal of Microelectronics and Packaging, Vol. 20, No. 2, 1997, pp. 81-88.

Giannakopoulos, A. E., Suresh, S., *Determination of elastoplastic properties by instrumented sharp indentation*, Scripta Materialia, Vol. 40, No. 10, 1999, pp. 1191-1198.

Grivas, D., Murty, K. L., Morris, J. W., *Deformation of Pb/Sn eutectic alloys at relatively high strain rates*, Acta Met. Vol. 27, 1979, pp. 731-737.

Hacke, P. L., Sprecher, A. F., Conrad, H., *Microstructural coarsening during thermo-mechanical fatigue of Pb-Sn solder joints*, Journal of Electronic Materials, Vol. 26, 1997, pp. 774-782.

Hall, P. M., *Creep and stress relaxation in solder joints of surface-mounted chip carriers*, IEEE Trans. CHMT, Vol. 12, No. 4, pp. 556-565.

Han, B., *Deformation mechanism of two phase solder column interconnections under highly accelerated thermal cycling condition: an experimental study*, ASME Journal of Electronics Packaging, Vol. 119, No. 3, 1997, pp. 189-196.

Haswell, P., *Durability assessment and microstructural observations of selected solder alloys*, Ph.D. Dissertation, Dept. of Mechanical Engineering, University of Maryland, College Park, MD, 2001.

Hertzberg, R. W., *Deformation and fracture mechanics of engineering materials*, Wiley, New York, 2nd Edition, 1983.

Hong, B. Z., Burrell, L. G., *Nonlinear finite element simulation of thermoviscoplastic deformation of C4 solder joints in high density packaging under thermal cycling*, IEEE CPMT A., Vol. 18, June 1995, pp. 585-591.

Huang, M. L., Wang, L., Wu, C. M. L., *Creep Behavior of eutectic Sn-Ag lead-free solder alloy*, Journal of Materials Research, Vol. 17, No. 11, Nov 2002.

Hwang, J., *Modern solder technology for competitive electronics manufacturing*, McGraw-Hill, New York, 1996.

Iosipescu, N., *New Accurate Procedure for Single Shear Testing of Metals*, Journal of Materials, Vol. 2, No. 3, September 1967, pp. 537-566.

JEDEC (Joint Electronic Device Engineering Council) Standard, *Temperature Cycling*, JESD22-A104-A, Electronic Industries Association, 1989, USA.

JEDEC (Joint Electronic Device Engineering Council) Standard, *Thermal Shock*, JESD22-A106-A, Electronic Industries Association, 1995, USA.

Jones, W. K., Liu, Y. Q., Zampino, M. A., Gonzalez, G. L., *The at-temperature mechanical properties of lead-tin based alloys*, Advancing microelectronics, 1997, pp. 30-34.

Kashyap, B. P., Murty, G. S., *Experimental constitutive relations for the high temperature deformation of a Pb-Sn eutectic alloy*, Materials Science and Engineering, Vol. 50, 1981, pp. 205-213.

Kay, P., McKay, C. A., *Barrier layer against diffusion*, Trans. Inst. Met. Fin., Vol.57, 1979, pp. 169.

Kilinski, T. J., Lesniak, J. R., Sandor, B. I., *Modern approaches to fatigue life prediction of SMT solder joints*, Solder Joint Reliability – Theory and applications, ed. Lau, Van Nostrand Reinhold, New York, 1991, pp. 384-390.

Knecht, S., Fox, L. R., *Constitutive relation and creep-fatigue life model for eutectic Tin-lead solder*, IEEE Trans. on CHMT, Vol. 13, No.2, 1990, pp. 424-431.

Kwon, S., Lee, Y., Han, B., *Constitutive Relationships of Binary Lead-free Solders*, Project C02-07, CALCE Consortium Report, October 2002.

Kwon, S., Lee, Y., Han, B., *Advanced Micro Shear Testing for Solder Alloy Using Direct Local Measurement*, Proceedings of IPACK'03, InterPACK2003-35325, Maui, Hawaii, (July 2003).

Lam, S. T., Arieli, A., Mukherjee, *Superplastic behavior of Pb-Sn eutectic alloy*, Materials Science Eng. Vol. 40, 1979, pp. 241-247.

Langdon, T. G., Mohamed, F. A., *The activation energies of superplasticity*, Scripta Metallurgica, Vol. 11, 1977, pp. 575-579.

Lau, J. H., Rice, D. W., *Thermal life prediction of flip-chip solder joints by fracture mechanics method*, AME Advances in Electronic Packaging, 1992, pp. 385-392.

Lee, Y., Kwon, S., Han, B., *Constitutive Relationships of Binary Lead-free Solders*, Project C02-07, CALCE Consortium Technical Review Meeting, March 2002.

Lee, Y., Kwon, S., Han, B., *Constitutive Relationships of Binary Lead-free Solders*, Project C02-07, CALCE Consortium Technical Review Meeting, October 2002.

Li, J., Dasgupta, D., *Failure-mechanism models for creep and creep rupture*, IEEE Trans. on Reliability, Vol. 42, No. 3, Sept 1993, pp. 339-353.

Mahidhara, R. K., Murty, K. L., Haggag, F. M., *Mechanical property characterization of Sn-5%Sb solder using traditional (tensile and creep) and ball indentation testing using stress-strain microprobe*, Proc. of Nepcon West 1996, Anaheim, CA, 1996, pp. 183-194.

Mavoori, H, Chin, J, Vaynman, S, Moran, B, Keer, L, Fine, M, *Creep, Stress Relaxation, and Plastic Deformation in Sn-Ag and Sn-Zn Eutectic Solders*, Journal of Electronics Materials, Vol. 26, No. 7, 1997.

McCluskey, F. P., Condra, L., Torri, T., Fink, J., *Packaging reliability for high temperature electronics: a material focus*, Microelectronics International, no. 41, Part III, 1994, pp. 3-10.

McCluskey, F. P., Grzybowski, R., Podlesak, T., *High temperature electronics*, CRC Press, Boca Raton, FL, 1997.

Mei, Z., Morris Jr., J. W., Shine, M. C., *Superplastic creep eutectic tin-lead solder joints*, Journal of electronics packaging, Vol. 113, 1991, pp. 109-114.

Meyers, M. A., Chawla, K. K., *Mechanical metallurgy, principles and applications,* Prentice-Hall, 1984.

Morris Jr., J. W., Tribula, D., Summers, T. S. E., Grivas, D., *The role of microstructure in thermal fatigue of Pb-Sn solder joints*, Solder Joint Reliability – Theory and applications, ed. Lau, Van Nostrand Reinhold, New York, 1991, pp. 225-265.

Mukai, M., Kawakami, T., Hiruta, Y., *Takahashi, K., Kishimoto, K., Shibuya, T., Fatigue life estimation of solder joints in SMT-PGA packages*, ASME Journal of Electronic Packaging, June 1998, pp. 207-212.

Personal Communication; Yuri Lee.

Pao, Y. H., Badgley, S., Jih, E., Govila, R., Browning, J., *Constitutive behavior and low cycle thermal fatigue of 97Sn3Cu solder joints*, ASME Journal of Electronics Packaging, Vol. 115, No. 6, 1993, pp. 147-152.

Raeder, C., H., Schmeelk, G. D., Mitlin, D., Barbieri, Yang, T., Felton, L. F., Messler, R. W., Knorr, D. B., Lee, D., *Isothermal creep of eutectic SnBi and SnAg solder and solder joints*, IEEE CPMT International Manuf. Tech. Symp., La Jolla, CA, September 1994, pp. 1-6.

Reinikainen, T., Ren, W., *An optimized shear test sample for assessing solder deformation properties*, Proceedings of EuroSimE 2001, Paris, April 2001.

Sandor, B., Ju, S. H., Plesha, M. E., *Life prediction of solder joints by damage and fracture mechanics*, ASME Journal of Electronics Packaging, Vol. 118, 1996, pp. 193-200.

Scandurra, A., Licciardello, A., Torrisi, A., La Mantia, A., Puglisi, O., *Fatigue Failure in Pb-Sn-Ag alloy during plastic deformation: A 3-D SIMS imaging study*, Journal of Materials Research, Vol. 7, No. 9, Sep 1992.

Schaffer, J., Saxena, A., Antolovich, S., Sanders Jr., T., Warner, S., *The science and design of engineering materials*, McGraw-Hill, New York, 1999.

Schubert, A., Walter, H., Dudek, R., Michel, B., Lefranc, G., Otto, J., Mitic, G., *Thermo-mechanical properties and creep deformation of lead-containing and lead-free solders*, Proc. of International symposium on advanced packaging materials: Processes, Properties and Interfaces, March 2001, pp. 129-134.

Shi, X. Q., Pang, H. L. J., Zhou, W., Wang, Z. P., *Temperature and Strain Rate Effect on Mechanical Properties of 63Sn/37Pb Solder Alloy*, WWP-Vol. 26-1, Advances in Electronic Packaging, Volume 1, ASME 1999.

Shi, X., Yang, Q., Wang, Z., Xie, D., Shi, Z., *New creep constitutive relationship and modified energy-based life prediction model for eutectic solder alloys*, SIMTech Technical Report (PT/01/021/JT), 2001.

Shine, M. C., Fox, L. R., *Fatigue of solder joints in surface mount devices*, Low Cycle Fatigue, Solomon, Halford, Kaisand, Leis (eds.), ASTM STP 942, 1988.

Skipor, A. F., Harren, S. V., Botsis, J., *On the constitutive response of 63/37 Sn/Pb eutectic solder*, ASME Journal of engineering materials and technology, Vol. 118, 1996, pp. 1-11.

Solomon, H. D., *Creep and strain rate sensitivity of a high Pb content solder with comparisons to 60Sn/40Pb solder*, Journal of electronic materials, Vol. 19, No. 9, Sept 1990, pp. 926-936.

Solomon, H. D., *Low cycle fatigue of surface mounted chip carrier/printed wiring board joints*, Proc. IEEE 39th ECC, 1989, pp. 277-292.

Tien, J. K., Hendrix, B. C., Attarwala, A. I., *Understanding the cyclic mechanical behavior of lead/tin solder*, Journal of electronics packaging, Vol. 113, 1991, pp. 115-120.

Tribula, D., Morris Jr., J. W., *Creep in shear of experimental solder joints*, Journal of electronics packaging, Vol. 112, 1990, pp. 87-93.

Tu, P. L., Chan, Y. C., Hung, K. C., Lai, J. K. L., *Growth kinetics of intermetallic compounds in chip scale package solder joint*, Scripta Materialia, Vol.2, No.44, 2001, pp. 317-323.

Vaynman, S., Fine, M. E., *Fatigue of low-tin lead-based and tin-lead eutectic solders*, Microelectronic Packaging Technology, ed. Shieh, W. T., 1989, pp. 225-259.

Veidt, M., *Viscoelastic tensile and shear properties of the 62wt%Sn-36wt%Pb-2wt%Ag solder alloy*, Journal of Materials Science, Vol. 33, 1998, pp. 1607-1610.

Wang, J., Qian, Z, Zou, D., Liu, S., *Creep behavior of a flip-chip package by both FEM modeling and real-time moiré interferometry,* ASME Journal of Electronics Packaging, Vol. 120, 1998, pp. 179-185.

Weertman, J., *An empirical relation defining the stress dependence of minimum creep rate in metals*, Trans. AIME, Vol. 227, 1963, pp. 1474-1477.

Wen, S., Keer, L., Vaynman, S., Lawson, L., *A constitutive model for a high lead solder*, IEEE Trans. on Comp. Packag. And Tech., Vol. 25, no. 1, March 2002, pp. 23-31.

Wiese, S., Schubert, A., Walter, H., Dukek, R., Feustel, F., Meusel, E., Michel, B., *Constitutive behavior of lead-free solders vs. lead-containing solders-experiments on bulk specimens and flip-chip joints*, Proc. of the 51st ECTC, June 2001, pp. 890-902.

Wilcox, J. R., Subrahmanyan, R., Li, C. –Y., *Assembly stiffness and failure criterion considerations in solder joint fatigue*, ASME Journal of Electronic Packaging, Vol. 112, No. 2, 1990, pp. 115-122.

Wilde, J., Becker, K., Thoben, M., Blum, W., Jupitz, T., Wang, G., Cheng, Z., *Rate dependent constitutive relations based on Anand model for 92.5Pb5Sn2.5Ag solder*, IEEE Trans. on Adv. Packag., Vol. 23, No. 3, August 2000, pp. 408-414.

Wong, B., Helling, D., Clark, R. W., *A creep-rupture model for two phase eutectic solders*, IEEE Trans. on CHMT, Vol. 11, 1988, pp. 305-325.

Yang, D., Pang, S., *Stress-strain analysis of single-lap composite joints under tension*, ASME Journal of Engineering Materials and Technology, Vol. 118, 1996, pp. 247-255.

Yang, H, Deane, P., Magill, P., Linga Murty, K., *Creep deformation of 96.5Sn3.5Ag solder joints in a flip chip package*, Proc. of IEEE ECTC, Orlando, FL, May 1996, pp. 1136-1142.

Zhang, Q., Dasgupta, A., Haswell, P., *Viscoplastic constitutive properties and energy-partitioning model of lead-free Sn3.9Ag0.6Cu solder alloy*, Proc. of the 53rd Electronic Components and Technology Conference, 2003. May 27-30, 2003, Page(s): 1862 -1868.